Icarus 419 (2024) 115863

Contents lists available at ScienceDirect

Icarus

journal homepage: www.elsevier.com/locate/icarus

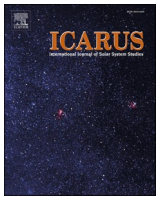

Revelations of interannual dune evolution from the swiftest aeolian system on Mars by MRO/HiRISE long-term monitoring

Matthew Chojnacki [a,*], David A. Vaz [b], Pruthviraj J. Acharya [c], Simone Silvestro [d,e], Isaac B. Smith [a,c]

[a] Planetary Science Institute, Lakewood, CO, USA
[b] Centre for Earth and Space Research of the University of Coimbra, Observatório Geofísico e Astronómico da Universidade de Coimbra, Coimbra, Portugal
[c] York University, Toronto, Ontario, Canada
[d] SETI Institute, Carl Sagan Center, Mountain View, CA, USA
[e] INAF Osservatorio Astronomico di Capodimonte, Napoli, Italy

ARTICLE INFO

Keywords:
Mars
Aeolian
Dune migration
Sand flux
Cryospheric processes

ABSTRACT

The north polar region of Mars, with its greater atmospheric pressure and vast inventory of ever-changing volatiles (e.g., CO_2, H_2O), hosts arguably the most active and diverse aeolian bedform systems on the planet. Here, we explore how these dune fields evolve spatiotemporally using up to 8 Mars years (16 Earth years) of MRO HiRISE observations to test the impact of various boundary conditions on annual mobility. A high degree of sand flux heterogeneity was observed for some dunes, whereas other sites displayed steady-state migration relative to long-term rates. These large changes in annual migration are attributed to the variable length of the frost-free seasons, sediment availability in relation to the timing of peak katabatic winds, and the influence of global dust storms on seasonal ice thickness. Consistent with our previous work, we continue to observe extremely high transport rates at Olympia Cavi. All stages of aeolian system evolution are observable (sand patch > protodune > dune), along with additional phenomena not previously observed outside of terrestrial settings (e.g., dune calving and collisions, remote transfer). Transitory protodunes may evolve from modest sand mounds to prominent barchans with slipfaces several meters tall within 3–5 Mars years, while adjacent duneforms may suffer slipfaces collapse as they lose sand supply. These Martian protodunes, which appear to be larger than terrestrial equivalents, and mature dunes found downwind are among the swiftest yet reported on Mars. These rapidly evolving cryo-aeolian systems provide a window into longer-term landscape evolution of non-polar dune fields.

1. Introduction and motivation

Driven by the cycles of insolation and volatiles that affect atmospheric pressure, winds frequently transport sediments across the surface of Mars today, as evidenced by the mobility of aeolian bedforms (Sullivan et al., 2008; Silvestro et al., 2010; Bridges et al., 2012). In particular, the north polar region with its lower elevation, greater atmospheric pressure, and vast inventory of ever-changing volatiles hosts some of the most active and diverse aeolian systems on Mars (Chojnacki et al., 2019, 2021; Diniega et al., 2022). For example, many initial detections of dune, ripple, and megaripple migration on Mars were associated with the aeolian systems surrounding the polar cap (Bourke et al., 2008; Hansen et al., 2011; Bridges et al., 2011; Chojnacki et al., 2021). Although there are important implications regarding the degree and frequency of sand mobility (e.g., climate, dust cycles, seasonal frost, etc.), little is known about the year-to-year variability.

These polar locations, similar to deserts on Earth, host multiple aeolian bedform classes that are distinguished by their overall-scale (i.e., spacing and height) and particle size distribution (Bagnold, 1941; Greeley and Iversen, 1985; Wilson, 1973). Both planets possess sand dunes, decimeter-wavelength impact ripples, and the larger (decameter-wavelength), asymmetrical coarse-grained "megaripples" (Greeley et al., 1992; Lancaster, 2009; Sullivan et al., 2005, 2008; Bridges et al., 2013). On Mars, the sandy low-albedo areas are characterized by intermediate-scale ripples with meter-wavelengths, which are distinct from those found in terrestrial aeolian environments (Bridges et al.,

* Corresponding author at: Planetary Science Institute, 1546 Cole Blvd #120, Lakewood, CO 80401, USA.
E-mail address: mchojnacki@psi.edu (M. Chojnacki).

https://doi.org/10.1016/j.icarus.2023.115863
Received 17 May 2023; Received in revised form 28 August 2023; Accepted 7 November 2023
Available online 11 November 2023

2007; Vaz et al., 2017). Indeed, these bedforms emphasize the influence of planetary boundary conditions, including atmospheric properties, sediment supply and availability, grain size, and the local volatile cycle, in forming bedforms and shaping aeolian systems on Mars (Kocurek and Ewing, 2012; Lapotre et al., 2016; Sullivan and Kok, 2017; Chojnacki et al., 2019; Vaz et al., 2023).

With the advent of sustained surface operations, such as the Mars Science Laboratory Curiosity rover at Gale crater, regular monitoring has provided insight into local aeolian trends (Geissler et al., 2008; Sullivan et al., 2008, 2022; Baker et al., 2022). Some of these campaigns utilized high cadence change detection to deduce diurnal and seasonal trends in wind azimuth and relative strengths (e.g., Baker et al., 2018, 2022). These results provide an invaluable dataset for calibrating atmospheric modeling and sand transport modeling (e.g., fluid transport), yet the roving nature of these missions and their science objectives limits their insight into long-baseline trends or other Martian aeolian systems outside of their paths.

More widespread and geographically-variable bedform activity has been afforded by repeat high resolution orbital images and topography from High Resolution Imaging Science Experiment (HiRISE) camera (0.25–1 m/pix) (McEwen et al., 2007). Prior HiRISE surveys of bedforms have shown variable activity across Mars, but the majority of studies have focused on repeat observations with sufficient duration to detect changes (2–4 Mars years) (Bridges et al., 2013; Chojnacki et al., 2015; Banks et al., 2018). While these approaches demonstrate general trends in regional aeolian changes, they fail to capture any interannual or seasonal variability in the winds. The few studies that utilized seasonal HiRISE observations of Martian bedforms have provided important constraints for sand transport physics (e.g., effective threshold) and atmospheric models (Ayoub et al., 2014; Roback et al., 2022). Nevertheless, these studies have been limited in terms of location (Nili and Meroe Patera) and time range (~1–3 Mars years).

Critically, HiRISE and its orbital platform Mars Reconnaissance Orbiter (MRO) (Zurek and Smrekar, 2007) have been operating near continuously from 2006 up until the writing of this report, which equates to nearly 8 Mars years of monitoring (Mars Year (MY) 28–36). This time period includes two planet-encircling dust events (2007 and 2018) and numerous smaller, episodic polar storms over that duration (Wang and Fisher, 2009; Cantor et al., 2019; Acharya et al., 2023). Of particular importance for north polar dunes is the recession rate of the seasonal polar cap, which has also being studied using MRO instruments (Calvin et al., 2015; Acharya et al., 2023), as that seasonal ice covers the circum-polar sand sea and restricts sediment transport by prohibiting grain movement. Indeed, the MRO polar orbit, with inclination of ~87° ensures many opportunities to image and scan areas poleward of about 60°, allowing interannual monitoring of every spring-summer sequence since 2006 (Russell et al., 2008; Hansen et al., 2015; Diniega et al., 2021; Chojnacki et al., 2021).

Along with seasonal cryospheric processes that drive landscape evolution across the polar latitudes, the atmospheric surface interactions are particularly tumultuous and acute along the margins of the north polar cap where steep slopes accelerate the winds (Wang and Fisher, 2009; Smith and Spiga, 2018). These intriguing areas host what have been suggested to be the swiftest bedforms yet detected on Mars using earlier data (Chojnacki et al., 2019, 2021) and provide an opportune opportunity to characterize how aeolian systems evolve over longer periods of time. Some of these emerging dune fields also have the added benefit of being directly sourced by the polar layered deposit basal scarps found upslope and upwind of the ergs (Fishbaugh and Head, 2005; Nerozzi and Holt, 2019) – thus, allowing source-to-sink systems to be examined.

Here we seek to provide insight into how Martian aeolian bedform systems evolve under the present-day north polar climate, with relevant questions such as: What are the annual variations in bedform migration and sand fluxes and how do those compare with long-baseline measurements? Are their examples of steady state or episodic migration, and what might be the driving factors? Does the time of spring CO_2 defrosting across the erg impact dune transport rates? How do dunes, ripples, and megaripples form and evolve from sand source to a mature aeolian system? To provide insight into these questions, our objectives are to 1) assess any annual variability in sediment flux over multiple Mars years and 2) better understand how polar aeolian systems evolve from incipient to mature bedforms. We will examine the objective's results in relation to the polar environment and how local boundary conditions affect bedform movement in the erg. This will help us gain a deeper understanding of wind processes in polar regions, assess annual or seasonal variations, and measure the changes in the landscape in a particularly dynamic area of Mars.

2. The north polar environment and annual factors

The north polar region of Mars is constantly changing due to various atmospheric and surface processes (see overviews by: Smith et al., 2018; Becerra et al., 2021; Landis et al., 2023). These processes are inherently linked to the phase changes of volatiles, particularly carbon dioxide, and the transport of dust between the polar and non-polar region (Langevin, 2005; Khayat et al., 2019). Whereas the northern polar cap is primarily made of 2 km of H_2O ice and dust overlying a ~ 1-km-thick basal unit composed of sand and ice, thin layers of CO_2 ice and frost permeate these high latitudes on a seasonal basis, covering the landscape with one to two meters of dense frost in winter and spring. The exchange between the surface and atmosphere causes various phenomena such as the formation of wind streaks (Howard, 2000), seasonal changes in albedo (Calvin et al., 2015), evolution of spiral troughs (Smith and Holt, 2010; Smith et al., 2013), generation of dust storms (Wang and Fisher, 2009), and avalanching of dune slipfaces (Hansen et al., 2011; Horgan and Bell, 2012; Diniega et al., 2017). The aeolian systems near the north polar layered deposits (NPLD) and residual cap (Fenton, 2020; Hayward, 2011) are primarily shaped by winds that are deflected by the Coriolis force (Ewing et al., 2010), flowing down into a series of ice-covered valleys or reentrant chasmata (e.g., Chasma Boreale, Olympia Cavi) (Howard, 2000; Fishbaugh and Head, 2005; Tanaka et al., 2008; Smith and Spiga, 2018). These ice cap reentrants provide an erosional window into the polar deposits and expose the ultimate source for the polar erg, which is widely recognized as the Planum Boreum Cavi and Rupes basal units - hereafter referred to as the Cavi or basal units (Thomas and Weitz, 1989; Byrne and Murray, 2002; Fishbaugh and Head, 2005; Nerozzi and Holt, 2019).

The polar erg sand becomes largely frozen and immobile during the northern autumn and winter following burial by CO_2 and H_2O ice which then slowly defrosts via sublimation during the spring, allowing the bedforms to become mobile again (Ewing et al., 2010; Hansen et al., 2011). Despite this seasonally controlled activity, which reduces the mobility period to less than half of the year, there is still a significant amount of aeolian transport during frost-free periods. These include the migration of meter-scale ripples, megaripples, and dunes (Bourke et al., 2008; Bridges et al., 2011; Hansen et al., 2011; Chojnacki et al., 2019, 2021).

In contrast to migrating megaripples, larger bedforms referred to as transverse aeolian ridges (TARs; 10–100 m spacing and 1–14 m tall) (Balme et al., 2008; Geissler and Wilgus, 2017) were found to be static and inactive in the circumpolar erg (Chojnacki et al., 2021). Even older bedform classes appear to have been stabilized by ice, buried, and entered into the polar sedimentary record, as evidenced by cross-bedding, sand-ice foresets, and wholly-preserved paleo-bedforms found across the region (e.g., Chasma Boreale, Olympia Cavi) (Herkenhoff et al., 2007; Ewing et al., 2010; Brothers and Kocurek, 2018; Chojnacki et al., 2021; Nerozzi and Holt, 2019). These bedform remnants are prone to erosion from surface winds and mass-wasting, which may liberate sandy material for redistribution. Thus, sand for the modern polar erg originates from multi-generational (secondary or beyond) sources. The presence of aeolian cross-stratification, dune casts,

and ice-cemented bedforms across the region suggest that these aeolian systems played a significant role in polar climatic and geological history (Tanaka et al., 2008).

3. Data sets and methods

3.1. Dune migration and sand fluxes

To assess annual migration patterns, we mapped a selection of aeolian sites on corresponding HiRISE orthoimages and digital terrain models (DTMs). Terrain generation at 1 m/post and image orthorectification at 25–50 cm/pixel were accomplished using SOCET SET® BAE system photogrammetry software (Kirk et al., 2008; Sutton et al., 2022). Based on prior surveys (Chojnacki et al., 2019), these locations are known to host relatively swift dunes and have up to 8 annual images that were acquired in the northern summer ($\Delta L_s \approx 20°$), but on different Mars years (Table 1). As these locations had been earlier characterized using long-baseline image series (>4 Mars years) (Chojnacki et al., 2019, 2021), individual dunes were selected which had produced the highest rates for a given site, typically 1–3 m/Mars year. Although this approach disregards slower dunes that could be quantified over longer durations it was deemed necessary to ensure at least ~3–4 HiRISE pixels of dune crest displacement between annual images. Displacement measurements were recorded by manually mapping polylines along dune crests in GIS for each image in the time sequence (Fig. 1A-1B) (Vaz et al., 2017; Silvestro et al., 2020). From earlier trials (Chojnacki et al., 2022), we determined that sand flux measurements obtained from crests or lee-face bases did not change significantly (see Fig. S1 for a comparison). More critical factors were found to be the solar azimuth and illumination of the advancing slipfaces, such that measurements were not attempted within significant shadows. One complication is that north polar dune slipfaces can form alcoves which may cut back into the lee-face causing an upwind displacement of a brink line (Diniega et al., 2017) - these areas were not mapped. Rippled slipfaces are common and denote local longitudinal sediment transport along the slipfaces (Eastwood et al., 2012), therefore these were not mapped.

Misregistration and jitter artifacts in orthoimages (Sutton et al., 2022) may produce displacements particularly noticeable on bedrock areas. The magnitude of these displacements is usually small (< 1 m) and results in N-S stripe artifacts (e.g. Fig. S2 in Silvestro et al. (2016)). As this study utilized annual HiRISE time-series, this sometimes required the mapping of small displacements - thus, it becomes relevant to account for this source of uncertainty. To facilitate this, several ground control points on bedrock areas located near the mapped dunes' crest lines were mapped to account for any long-wavelength displacement patterns (Fig. S1). Sub-pixel correlation between the analyzed image pairs is used to estimate the apparent bedrock displacement. For each of the mapped lines average displacements were retrieved from the nearest ground control points (Fig. 1B, S1). The obtained average displacements are used to shift the polylines, correcting their locations and improving the accuracy of the flux estimates. Note this technique works best for dunes with lower sand supply, where inter-dune bedrock areas are frequent. Overall, for the four study sites we use a total of 4749 control points, with the magnitude of the residual displacements averaging to 0.7 ± 0.65 m.

Volumetric sand fluxes were then semiautomatically computed across the full extent of the slipfaces by multiplying the estimated heights and displacements over the intervening time (typically 1 Mars year) – see the method of (Urso et al., 2018). The process involves combining data from HiRISE orthoimages and DTMs to create continuous measurements of height and migration along slipfaces (Fig. 1C). Slipface heights were measured in the single time-step that

Table 1
Summary metrics[a] (average values) from annual monitoring of study dune fields[b]. Image details are provided in Table S1.

Image Pair	Elapsed time (EY/MY)	Migration rate (m/yr)	Flux ($m^3\ m^{-1}\ yr^{-1}$)	Height (m)	Height range (m)	DOA[b]: MY(L_s°)
1186+835_WestOlympia						
PSP_001712_ESP_053270_SF	11.0/5.8	0.3 ± 0.1	3.2 ± 1.2			28(147) – 34(98)
PSP_001712_PSP_010019_SF	1.8/0.9	0.4 ± 0.2	3.7 ± 1.7			28(147) – 29(127)
PSP_010019_ESP_019025_SF	1.9/1.0	0.3 ± 0.2	3.1 ± 2.1	11.1 ± 4.3	3.6–20.3	29(127) – 30(135)
ESP_019025_ESP_027728_SF	1.9/1.0	0.3 ± 0.1	2.5 ± 1.8			30(135) – 31(130)
ESP_027728_ESP_036299_SF	1.8/1.0	0.4 ± 0.2	3.7 ± 1.5			31(130) – 32(121)
ESP_036299_ESP_044686_SF	1.8/1.0	0.3 ± 0.1	2.8 ± 1.4			32(121) – 33(106)
ESP_044686_ESP_053270_SF	1.8/1.0	0.4 ± 0.1	3.4 ± 2.0			33(106) – 34(98)
2329+840_Buzzel						
PSP_009105_ESP_071057_SF	13.2/7.0	1.2 ± 0.6	10.5 ± 6.4			29(95) – 36(103)
PSP_009105_ESP_018427_SF	2.0/1.1	0.9 ± 0.5	6.9 ± 4.9			29(95) – 30(113)
ESP_018427_ESP_027394_SF	1.9/1.0	1.5 ± 0.6	12.0 ± 6.6			30(113) – 31(118)
ESP_027394_ESP_036176_SF	1.9/1.0	1.2 ± 0.9	8.9 ± 6.7			31(118) – 32(117)
ESP_036176_ESP_044352_SF	1.7/0.9	1.3 ± 1.0	9.4 ± 5.5	9.5 ± 3.8	2.4–17.4	32(117) – 33(94)
ESP_044352_ESP_053345_SF	1.9/1.0	1.3 ± 0.7	10.3 ± 5.5			33(94) – 34(100)
ESP_053345_ESP_062945_SF	2.0/1.1	1.3 ± 0.8	10.0 ± 7.2			34(100) – 35(128)
ESP_062945_ESP_071057_SF	1.7/0.9	1.3 ± 0.7	10.2 ± 6.1			35(128) – 36(103)
2365+838_OlympiaCavi						
ESP_018981_ESP_062866_SF	9.4/5.0	0.6 ± 0.4	3.5 ± 2.2			30(133) – 35(126)
ESP_018981_ESP_027539_SF	1.8/1.0	0.4 ± 0.3	3.0 ± 2.2	7.8 ± 2.9	1.1–16.1	30(133) – 31(123)
ESP_027539_ESP_037099_SF	2.0/1.1	0.6 ± 0.3	4.0 ± 2.0			31(123) – 32(152)
ESP_037099_ESP_062866_SF	5.5/2.9	0.4 ± 0.4	2.5 ± 1.8			32(152) – 35(126)
3393+850_ChasmaBoreale						
PSP_001374_ESP_071620_SF	15.0/8.0	0.4 ± 0.2	3.5 ± 1.4			28(134) – 36(123)
PSP_001374_PSP_010085_SF	1.9/1.0	0.7 ± 0.2	6.0 ± 2.3			28(134) – 29(130)
PSP_010085_ESP_036330_SF	5.6/3.0	0.3 ± 0.2	2.5 ± 1.5			29(130) – 32(122)
ESP_036330_ESP_045192_SF	1.9/1.0	0.6 ± 0.3	4.9 ± 2.3	9.9 ± 3.0	2.2–14.7	32(122) – 33(124)
ESP_045192_ESP_054013_SF	1.9/1.0	0.3 ± 0.2	2.8 ± 1.7			33(124) – 34(124)
ESP_054013_ESP_062664_SF	1.8/1.0	0.4 ± 0.4	3.5 ± 3.5			34(124) – 35(118)
ESP_062664_ESP_071620_SF	1.9/1.0	0.5 ± 0.4	3.4 ± 1.8			35(118) – 36(123)

[a] Long-baseline metrics are provided for each site on the top row.
[b] Date of Acquisition (DOA) ranges are provided in Mars years and solar longitude.

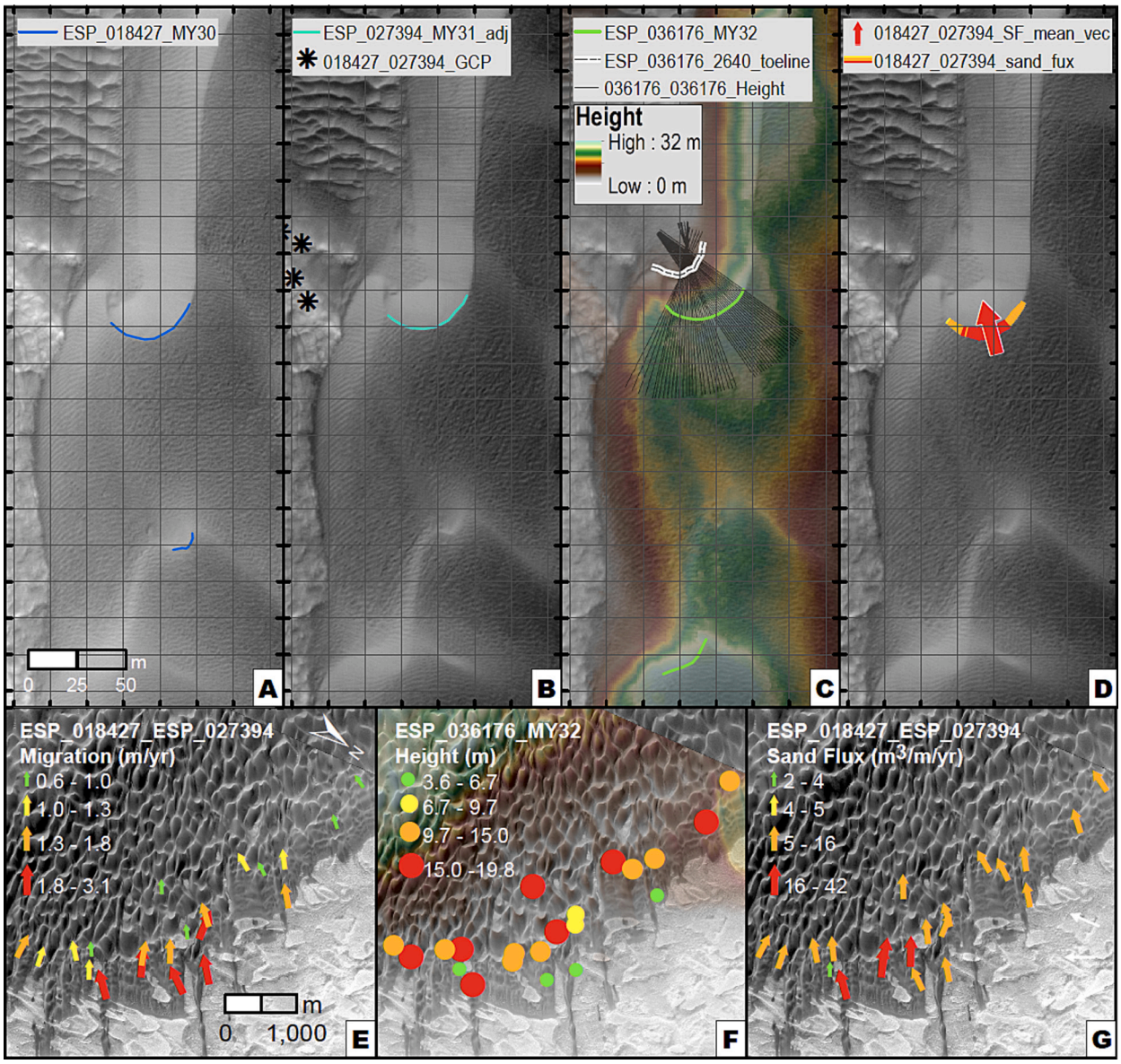

Fig. 1. Examples of the methodology of measuring dune migration, height, and sand flux on sand dunes in Olympia Cavi (site 2329+840_Buzzel). (A) Crest measurements of a single dune in the Mars year (MY) 30-time-step. Grid spacing for (A-D) is ~20 m. (B) Measurement of the same dune in MY31, where the ground control points (stars) were used to correct the location of the dune brinks from minor bedrock shifting between orthoimages. (C) Profiles used to derive dune heights from the crest and toe lines using the MY32 DTM and associated ortho. Colorized elevation from DTM DTEPC_036176_2640_035926_2640_A01. (D) The resulting MY30–31 sand flux measurements (green traces) and average flux vector magnitude "_SF_Mean_vec" (red circle). A wider view of the corresponding (E) migration rate, (F) dune height, and (G) sand flux metrics. (For interpretation of the references to colour in this figure legend, the reader is referred to the web version of this article.)

corresponded with the sites stereo and DTM. Although this was unavoidable without multiple terrain models, it is estimated that most dune heights are not likely to vary significantly (~10%) over these relatively short time periods - note that assumption was not extended for protodunes, which may show drastic changes in shape. Collectively, these measurements allowed annual and long-baseline volumetric sand fluxes ($m^3\ m^{-1}\ yr^{-1}$) to be calculated, along with displacement distance, migration rate, dune heights, and image pair details (Fig. 1E-G, Table 1). Metrics are reported in Earth years, while the elapsed time between images is typically given in Mars years. Although this approach produces lower average fluxes than studies taking spot/peak measurements of select dunes (Chojnacki et al., 2018), it provides a more precise depiction of the dune fluxes and can be compared with earlier studies that used a similar approach (Urso et al., 2018; Silvestro et al., 2020; Chojnacki et al., 2021). Although annual observations were the focus for this investigation, we also used springtime HiRISE images to better understand the dune defrosting sequences, consistent with prior work (Portyankina et al., 2013; Hansen et al., 2013, 2015; Diniega et al., 2017).

Animations were generated to provide additional insight into bedform evolution over annual time steps. GIF animations were built using in-house software which stacks orthophoto subsets in chronological order and provides relevant temporal and geographic context. As per convention, the solar longitude (L_s) range of 0°–360° defines a Mars Year (MY) and 11 April 1955 ($L_s = 0°$) is the start of the Mars calendar at MY01 (see Piqueux et al. (2015a) for details). Consistent with earlier work (Hayward, 2011; Chojnacki et al., 2018, 2019), study site IDs are given with coordinate location and a regional name (e.g., 1186+835_WestOlympia). The first four digits of the site IDs are the centroid's east longitude, the last three digits are the site's latitude (each coordinate given to the first decimal place without the decimal), and the

separating + indicating the northern hemisphere. Image, DTMs, and site details are listed in Table 1 and Supplementary Materials (SM) Table S1.

3.2. Annual erg defrost timing and seasonal wind simulation

The timing of seasonal defrosting across the north polar region may be critical for annual dune fluxes since CO_2 ice prevents sand grain transport. Using daily polar mosaics obtained from the Mars Color Imager (MARCI) (Bell et al., 2009), we investigated the defrosting "crocus" timing for each dune field from Mars year 29–35 and L_s 30° to L_s 105°. The crocus date denotes the last appearance of CO_2 frost following a sharp rise in surface temperature (Calvin et al., 2015). MARCI polar mosaics were converted from the standard Red, Green, and Blue (RGB) format to the Hue, Saturation, and Value (HSV) colour format, similar to Acharya et al. (2023) who constrained the retreat rates of the Northern Polar Seasonal Cap (NPSC). Subsequently, we recorded the average brightness (V value) of the pixel situated at the latitude and longitude coordinates of the four-dune fields, covering a region of 0.12° x 0.12° or roughly the area of a HiRISE image (7.3 km × 7.3 km). All the sites are situated away from ice cap areas and are therefore distinguishable from residual ice.

The goal of using every MARCI mosaic is to detect inter-seasonal trends while minimizing noise. This was accomplished through the implementation of a non-parametric smoothing technique, excluding approximately 20% of the data (e.g., low SNR, polar storms). To determine the crocus date of defrosting, we identified the L_s date when the mean brightness reaches the fastest rate of decrease for that year's spring. Then, using that L_s date, we verified the seasonal cap retreat timing in the corresponding MARCI mosaics, which marks the theoretical period when sand is defrosted. These MARCI-derived defrost dates can be further verified using higher resolution, but lower temporal frequency CTX or HiRISE images (Hansen et al., 2013; Portyankina et al., 2013; Diniega et al., 2017).

Finally, we compare our results from MARCI and sand flux analyses with prior mesoscale atmospheric modeling of the north polar region from Smith and Spiga (2018). Those Laboratoire de Météorologie Dynamique (LMD) Martian Mesoscale Model (MMM) based results provide context for the wind seasonality, in terms of magnitude, location, and timing (L_s 30°-140°).

4. Results

4.1. Dune migration and sand flux variability

Four dune fields were selected for multi-Mars year analysis, based on location and data availability (Fig. 2A). All these sites are located at the head of a polar reentrant, downwind of the aeolian system's sediment source (Fig. 2B), and had 3–7 annual time steps between Mars year 28 and 36 (Fig. 3), where long-baseline first to last image sand fluxes are mapped on Fig. 1C/1E/1G (also see Fig. S2). Unambiguous advancements of lee fronts are observed in all the image-pairs. Starting with the informally named West Olympia reentrant site (Table 1, Fig. S2, 1186+835_WestOlympia), this dune field context shows a common physiography of networked troughs, scarps, and depressions where alcove geometry impacts local sand transport. Here, Cavi units crop out along the lower slopes of the Planum Boreum exposing sand-rich source layers, which first form meter-scale dark ripples and larger TARs along mid-slope benches (Fig. 2C, 4 A)(see Fig. 9 of Tanaka et al., 2008). Downwind of these areas, dunes were tracked and found to have relatively low migration rates diagonal from the scarp (0.8–4.0 m^3m^{-1} yr^{-1}; azimuth 186°; Fig. 3I, S2A). However, as the aeolian system progresses south around the protruding edge of the alcove (Fig. 2D), migration rates increase where dunes veer more towards the southwest (1.9–5.5 m^3m^{-1} yr^{-1}; azimuth 224°) (Fig. 2C, inset; 4, S2). Median annual sand fluxes from Mars year 28 through MY34 fluctuated between 2.5 and 3.7 m^3m^{-1} yr^{-1} (Fig. 3A) and averaged 3.2 ± 1.2 m^3m^{-1} yr^{-1} over the 6-time steps (Table 1).

Moving eastward are two adjacent sites at the head of the Olympia Cavi reentrant (Fig. 2B). The first site (Table 1, 2329+840_Buzzel) is notable as numerous prior investigations have looked at various aspects of these dunes (e.g., defrosting sequence, sand composition, slumping, morphology, sand fluxes) (Pommerol et al., 2013; Portyankina et al., 2013; Hansen et al., 2013, 2015; Ewing et al., 2015; Diniega et al., 2017; Chojnacki et al., 2019, 2021). The dune field is set ~5 km downwind of the Planum Boreum and Cavi scarp units and is largely free of any prominent topography (Fig. 2E, 4B, S2B). Only low-relief, hummocky Cavi units mantled in sporadic sand sheets or TARs sit between the dunes and the sand source (Tanaka et al., 2008) in a transverse wind regime (Chojnacki et al., 2021). The scarp serves as a line sand source (Ewing and Kocurek, 2010), where dune migration to the southwest is roughly perpendicular to the Cavi scarp (Fig. 2F, 3J, 4B, S2B; azimuth 234°). Symmetric barchans and protodunes dominate the leading edge of the field (Animation 1) which gives way to larger barchanoid dunes as sediment supply increases downwind. Sand transport here is far greater than for most locations on Mars (Chojnacki et al., 2019, 2021) as dunes can be easily tracked advancing between 1 and 3 m/Mars year (average 1.2 m/Earth year). The "Buzzel" dune field sand fluxes averaged to 10 ± 6.8 m^3m^{-1} yr^{-1} over MY29–36 but varied significantly over the 7-time steps (Fig. 3B, F, Table 1, S1). A factor of two increase in fluxes occurred between the initial lowest (MY29–30) and preceding highest (MY30–31) transport years (Fig. 3B; 6.9 ± 4.9 vs. 12.0 ± 6.6 m^3m^{-1} yr^{-1}). These annual dune fluxes are consistent with earlier analysis of this field, but with a greater number of dunes and total field area (Chojnacki et al., 2021).

Twenty kilometers to the southeast is the 2365+838_OlympiaCavi dune field which has a similar geometry to the West Olympia site with a right flank (upwind) alcove scarp — although sand transport here is more variable and parallel to that scarp (Fig. 2F, 3K, 4C, S2; azimuth ~200°). Sand fluxes for this site are more typical for other sites on Mars where the HiRISE sequence covers the leading edge of a barchan-barchanoid dune field (Fig. 2E, S2B; average 3 ± 1.8 m^3m^{-1} yr^{-1}). Annual fluxes did not vary significantly over the 3-time step between MY30–36 (Fig. 3C; 2.5 ± 1.8 vs. 4.0 ± 2.0 m^3m^{-1} yr^{-1}).

The final reentrant site sits at the head of Chasma Boreale which is a well-known sand pathway into the polar erg (Byrne and Murray, 2002; Tanaka et al., 2008; Brothers and Kocurek, 2018; Li et al., 2018). The leading edge of the study dune field (3393+850_ChasmaBoreale) is downwind of the Boreum Cavi wall which is diagonal relative to the transport direction (Fig. 2G, S2D). Possibly related, there is a notable asymmetry in dune morphology where right-flank dunes are elongated along that side (Fig. 2H). Sand fluxes here were estimated for 6-time steps and averaged to 3.5 ± 1.4 m^3m^{-1} yr^{-1} between MY28–36 (Fig. 3L, Table 1; azimuth 223°). A notable decline occurred from the maximum MY28–29 rate of 6.0 ± 2.3 m^3m^{-1} yr^{-1} down to the series minimum 2.5 ± 1.5 m^3m^{-1} yr^{-1} in MY29–32 (Fig. 3D). The remaining image pairs did not vary significantly although the lowest single year fluxes occurred over MY34-MY35.

4.2. Dune field defrost timing from MARCI brightness values

MARCI brightness values provide insight into how surface ice evolve throughout the northern spring because the seasonal CO_2 frost is more reflective than the darker sand and basement material that it covers. The study sites situated at the head of the polar reentrant chasmata follow similar linear annual recession trends in brightness (Fig. 5, Table 2) to the larger seasonal cap at lower latitudes (Acharya et al., 2023). The dune fields reached their maximum rate of brightening and became frost free between L_s 75° and 85°. The 2365+838_OlympiaCavi site has the largest variation, where the average crocus dates was L_s 78.6° ± 2.8° (Fig. 5C); whereas 1186+835_WestOlympia has the smallest variation, with a consistent crocus date of L_s 77.2° ± 1.0° (Fig. 5A). The earliest defrosting estimate from MARCI was at L_s 75.4°

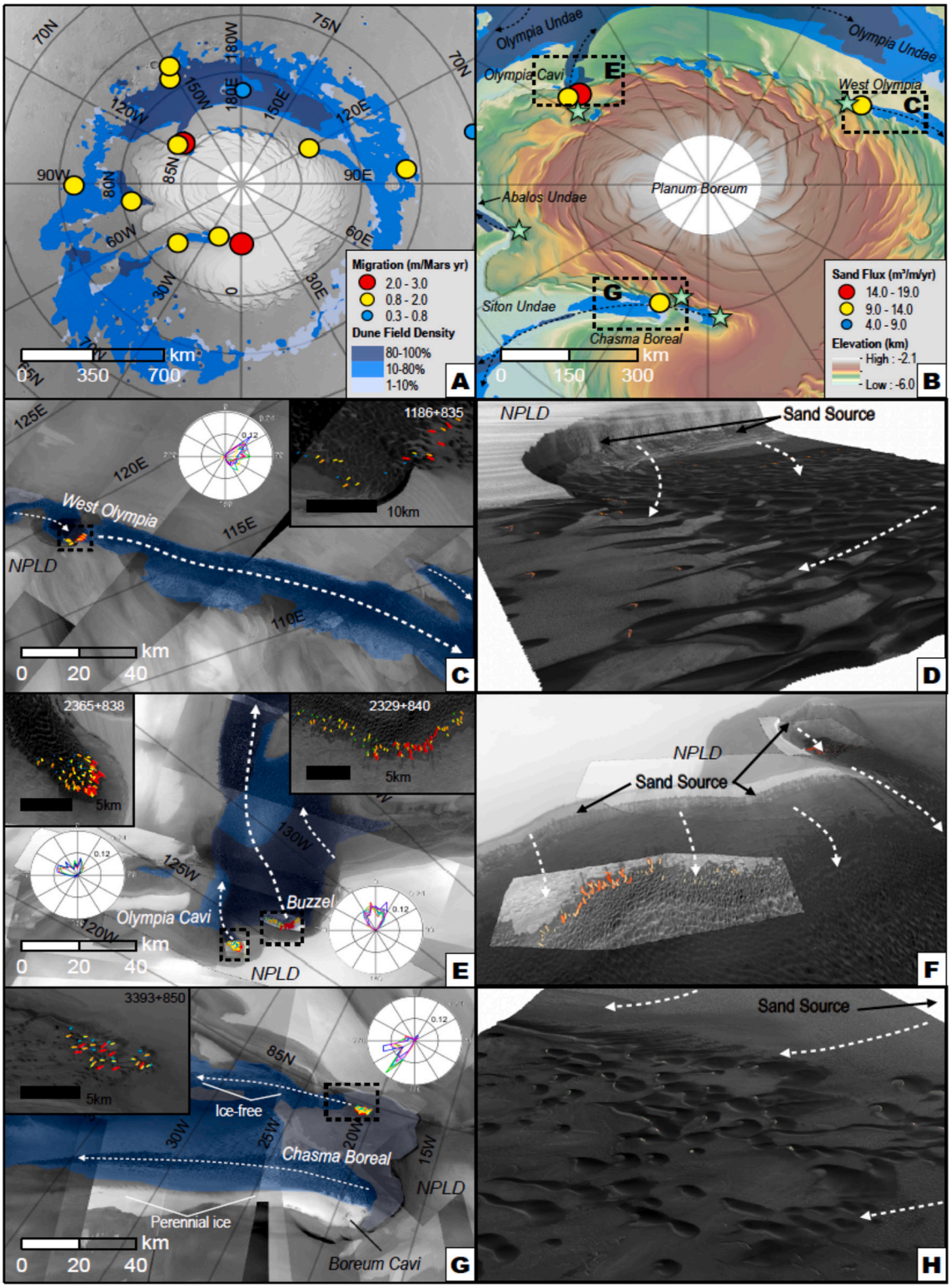

Fig. 2. Maps of the north polar erg showing study sites investigated herein. (A) Regional view of dune migration rates from Chojnacki et al. (2019, 2021) and (B) new sand flux results of dune fields studied herein (colored circles). The simplified transport directions (dashed arrows) and regional sand sources (green stars) within the 3 main reentrant chasmata are also viewable in (B). Base maps are MOLA shaded relief with grayscale or colorized elevation and dune field distribution are shown in blue (Hayward, 2011). (C, E, G) CTX mosaics of study sites with sand flux vectors (colored arrows), transport directions (white arrows) and look angles (orange arrows) for associated perspective views from (D, H) HiRISE and (F) CTX terrain models, where scale can be estimated from the width of HIRISE DTMs at ~5 km. Details for the sand flux rose diagrams (C, E, G) are provided in Fig. 3I-L. See Fig. S2 for closer views and 4 for perspective views. (For interpretation of the references to colour in this figure legend, the reader is referred to the web version of this article.)

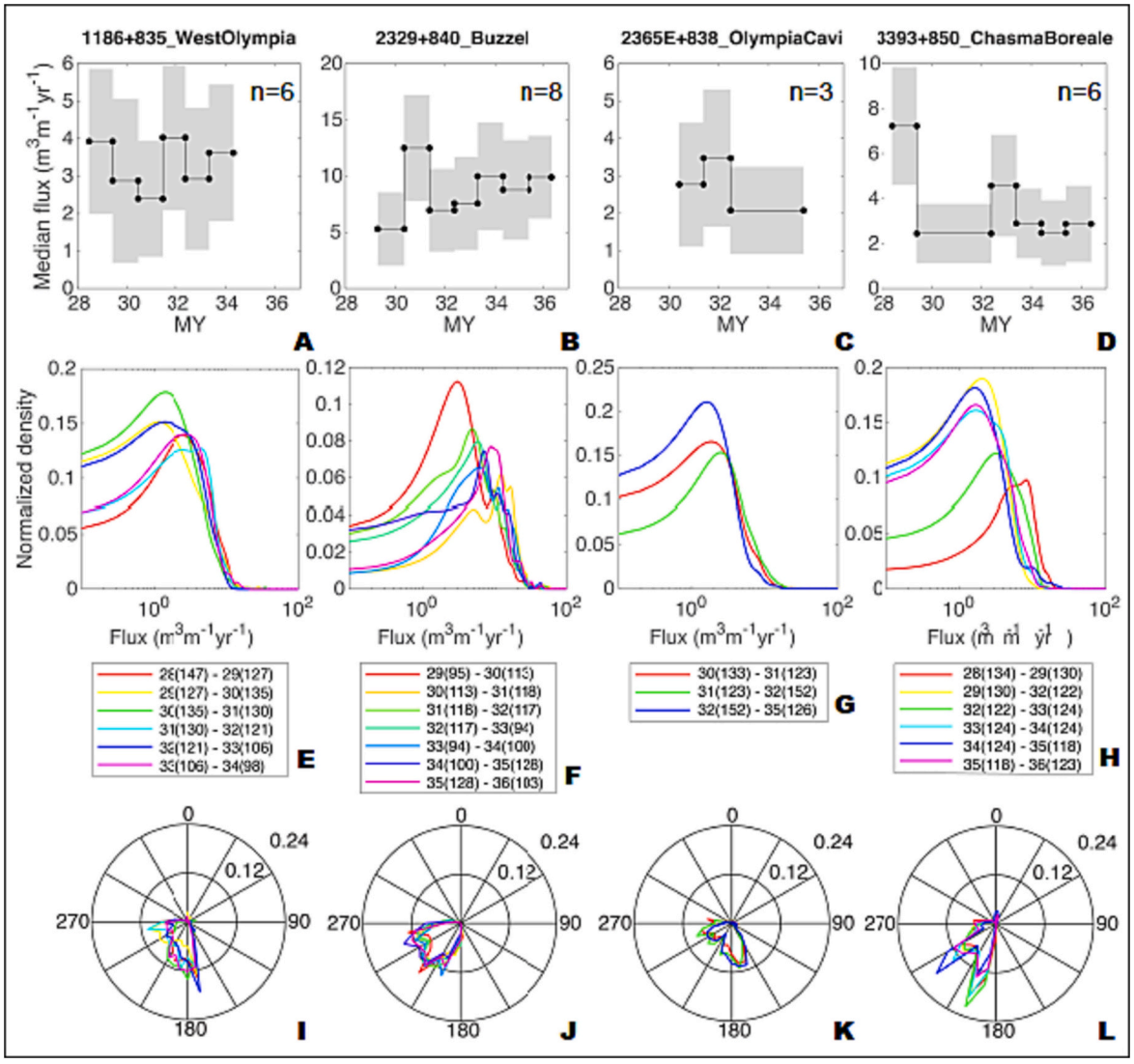

Fig. 3. Plots of annual dune dynamics for the 4 study sites with names at the top of each column. (A-D) Median sand fluxes plotted vs. time (Mars year (MY) 28–36) where circles correspond with measurements. Median absolute deviations are in gray. (*E*-H) Normalized density of annual sand fluxes. Colour key list shows the image pair timing in MY(L_s). Compare with Tables 1 & S1. (I-L) Circular rose plots showing the sand fluxes per image pair where azimuth is plotted relative to the geographical North. Same colour key as with 3E-3H. For rose plots oriented relative to image-up, see Fig. 2C, E, G. (For interpretation of the references to colour in this figure legend, the reader is referred to the web version of this article.)

(2365+838_OlympiaCavi), while the latest date was at L_s 84.3° (Fig. 5B; 2329+840_Buzzel).

For most sites, it was found that MY 29 and MY 35 were endmembers in terms of defrost dates compared to the MY 30–34 average. In general, MY 29 defrosts earlier, and MY 35 defrosts later, indicating that those two years experienced anomalies, possibly related to global dust storms (see section 5.1.2); however, the differences in the date were site-dependent. The MY 29 date was advanced by 2.2–3.2° of L_s, as compared to the MY 30–34 averages for those sites. Interestingly, all sites during MY 35 were lagging by ~1–5° L_s dates compared to averages.

4.3. Aeolian system evolution

Annual dune field observations over relatively long durations allow for bedform evolution trends to be assessed from source-to-sink. This is particularly true for the Buzzel site of the Olympia Cavi reentrant (Fig. 2E-2F), which shows some of the highest transport rates on Mars - dune migration rates of 5.4 m/yr and fluxes of 30–60 m^3m^{-1} yr^{-1} have been reported (Chojnacki et al., 2019, 2021).

Sand source areas are at the base of the NPLD and Cavi unit scarp wall (Fig. 4). Variably sized (10–70 m) blocks of the NPLD and basal unit, liberated by thermally-driven expansion and contraction, cascade onto lower slopes (Herkenhoff et al., 2007; Russell et al., 2008; Fanara et al., 2019; Su et al., 2023). The resulting fan-shaped deposits of blocks and dark sediment may evolve into bright, static TARs or isolated patches of dark sand, some of which can form active ripples (Fig. 4). Although there are some examples where sandy outcrops directly source protodunes or dunes (Fig. 4 A, 4B, Animation 7), many pathways between source and erg lack dunes (Fig. 4B, 4C). These latter dune-free corridors are expected to have regular sand transport into the erg throughout most of the frost-free seasons that is difficult to quantify with HiRISE (see below). Most bedform development occurs downrange.

The Initial stage of dune field development observed is the transition from sand patches to protodunes which occurs along a diffuse 1–2 km-long corridor of the aeolian system (Fig. 6A). Sediment that can be transported by saltation accumulates into isolated domal or elliptical shaped mounds or may develop into more concentrated lenses of linear trains. Coarser grained sediment may accumulate in topographic lows or on bedrock, eventually forming megaripples, where sand transport is

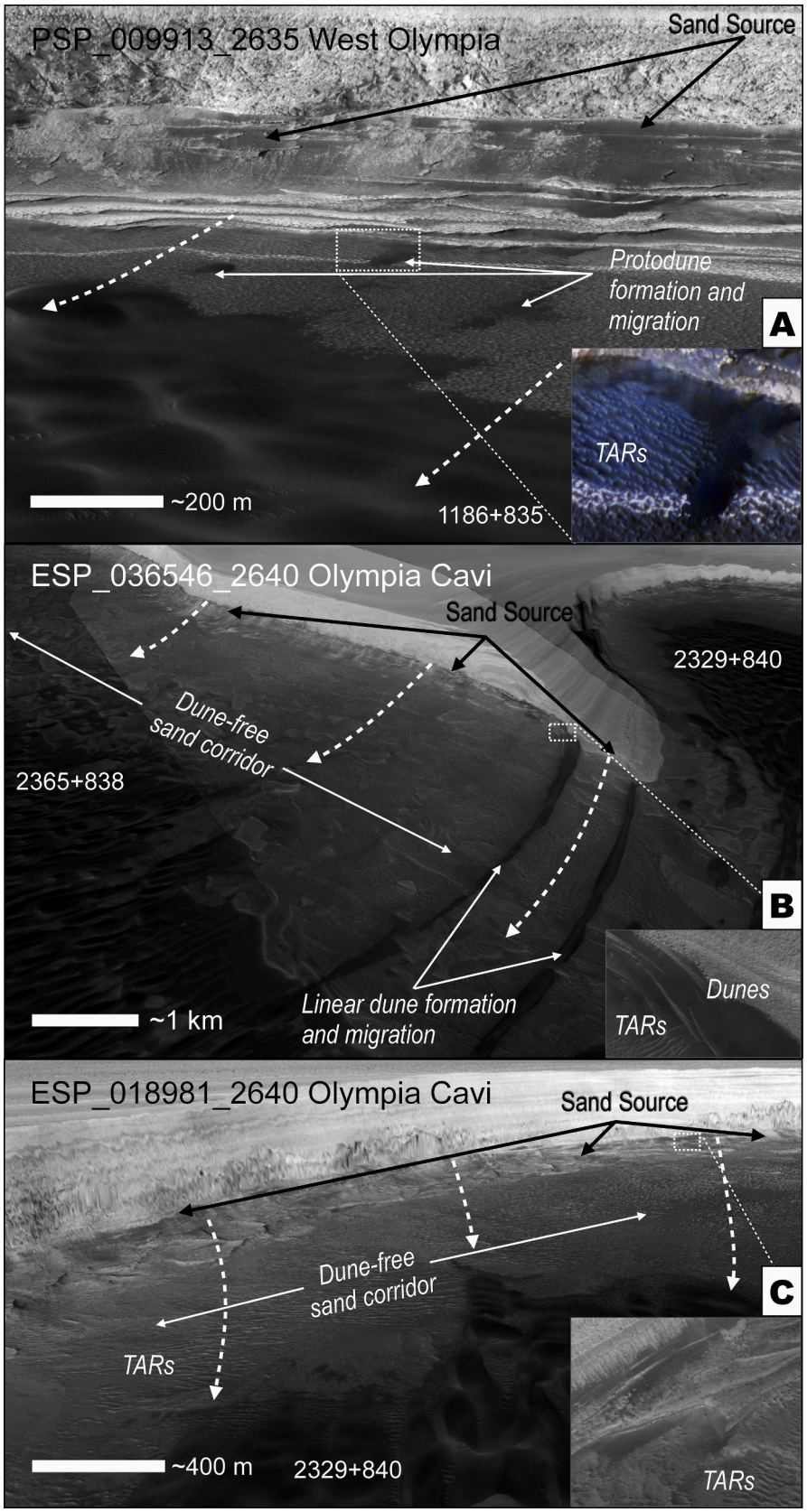

Fig. 4. Perspective views from (A, C) HiRISE and (B) CTX terrain models, showing sand source-to-sink details. Insets show HiRISE views of sand sources. Compare with Fig. 2D, 2F

Table 2
Dune field and the approximate crocus defrost dates for the location.

Data Collection Location	Site Name	MY 29 (L_s°)	MY 30 (L_s°)	MY 31 (L_s°)	MY 32 (L_s°)	MY 33 (L_s°)	MY 34 (L_s°)	MY 35 (L_s°)	Average MY29-MY35 (L_s°)
83.43°N, 119.14°E	WestOlympia	78.0	76.9	75.9	77.4	78.0	76.0	78.4*	77.2
83.92°N, 233.43°E	Buzzel	77.0*	79.5	79.3	78.9	78.7	79.7	84.3	79.6
83.77°N, 236.30°E	OlympiaCavi	75.4*	79.3*	78.4	77.1	80.9	76.1	83.3	78.6
84.95°N, 339.08°E	ChasmaBoreale	76.5	78.3	77.4	78.3	79.2	78.3	82.7	78.7

* No sand flux measurements at this site for this Mars year.

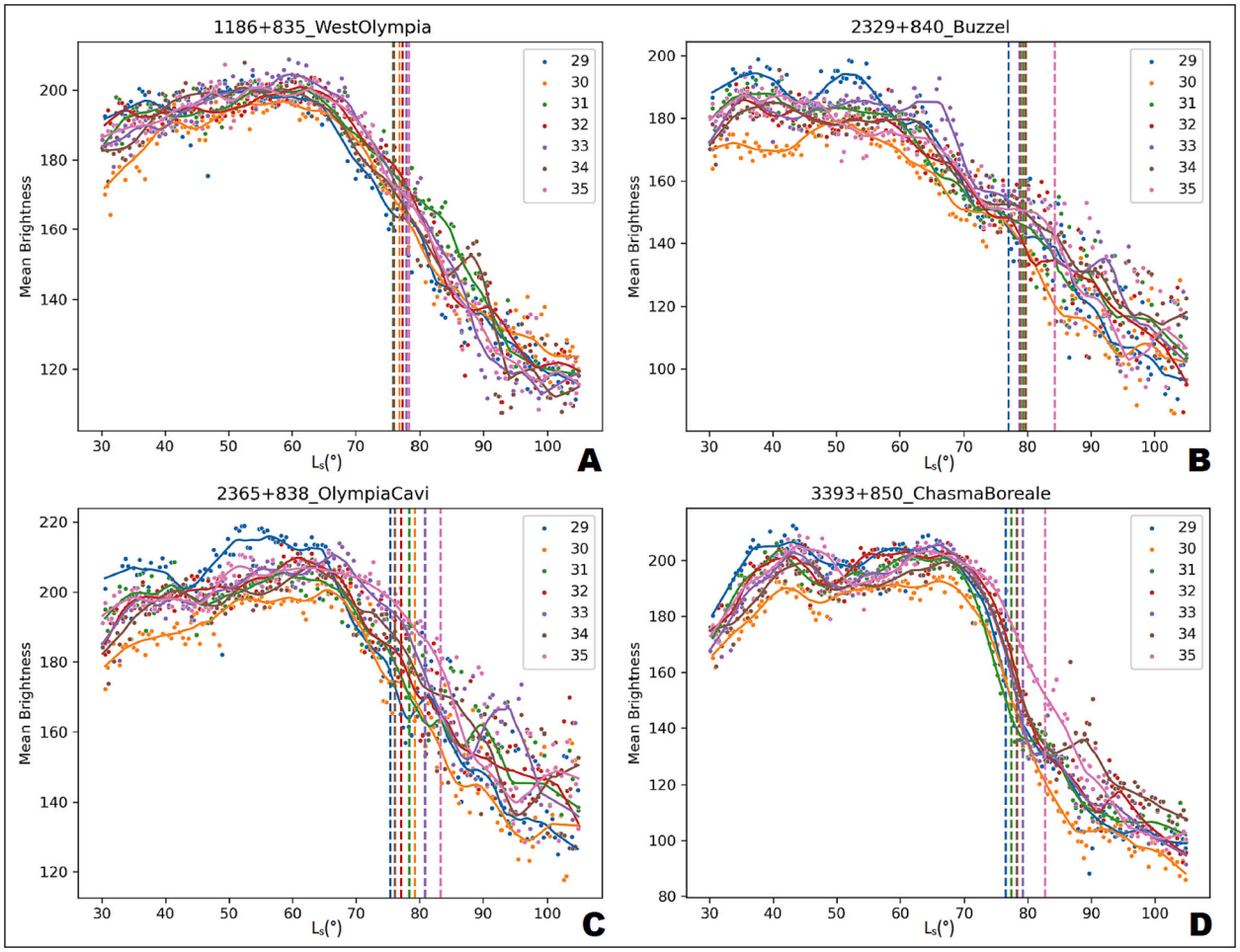

Fig. 5. MARCI mean brightness vs. solar longitude for the four dune field sites for Mars years 29–35. The vertical lines represent the solar longitude of maximum brightening (exact dates found in Table 2) for a given Mars year, which approximates when frost-free dune sediment becomes available for transport.

abundant. Low-relief (~1–6 m tall) protodunes with 75–200 m wavelengths rapidly migrate across the corridor climbing up or descending the hummocky polar terrain, including 10–40 m tall scarps (Fig. 7, Animation 1). Even small dark-toned patches or sheets exhibit meter-scale ripples, where ripple definition and wavelength tend to increase with patch area. However, not all sand transport is evident in HiRISE images. Protodunes are frequently disrupted by the underlying topography, which appears to impact bedform coherence and cause calving of new bedforms. Fig. 6B (also see Animation 3) shows an example of one such calving protodune, where areas directly downwind of a topographic step darken and eventually accumulate ripples over several Mars years. These new ripple patches often form on rough terrain that serve as nucleation sites. This example (Fig. 6B, Animation 3) denotes the occurrence of the remote transfer of sediment (Kocurek et al., 2010) that is unresolved by HiRISE (i.e., sub-pixel), due to the meter-scale ripple formation along with megaripple migration observed downwind. Transport would occur most likely via centimeters-scale impact ripples (Sullivan et al., 2005, 2022; Baker et al., 2018, 2022) or saltation "splash" clouds during high wind events (Sullivan and Kok, 2017). This is not necessarily a surprising revelation as this site lacks resolvable sand patches in the kilometers of polar terrain separating the sand source and erg margin (Fig. S3A), yet the protodunes emerge and grow annually indicating some regular input. Additionally, the migrating megaripples located on bedrock and not in contact with dark-toned ripples are consistent with this notion since saltation-induced reptation events are the likely driver of their mobility (Fig. 6B, S3A, Animation 3) to develop steeper lee slopes where grain flow may occur (Fig. 7, 8, Animation 4–5). Over a few Mars years these slopes steepen, expand, and form angle of

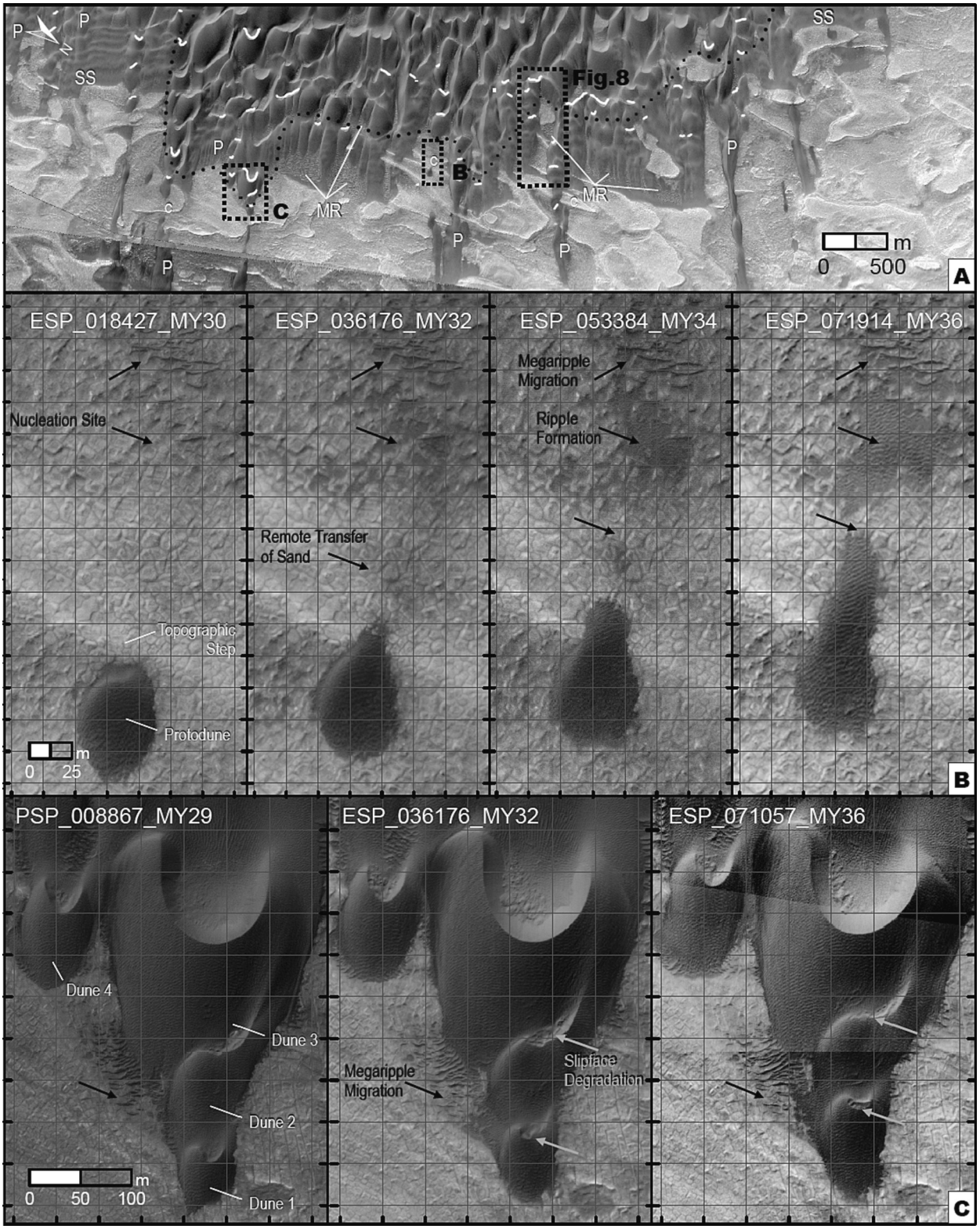

Fig. 6. Various stages of bedform evolution. (A) Context of the leading (upwind) edge of the Olympia Cavi reentrant aeolian system or "Buzzel" dune site. P = protodunes, SS = sand sheets, MR-megaripples, c = calving event. Select dune crests are annotated. The dotted line denotes the diffuse boundary between (bottom) protodunes and (top) mature dunes. (B) The partial fragmentation of one protodune, where sediment is remotely transferred downwind to a new ripple patch. Grid spacing is ~20 m. (C) A series of dune interactions at upwind margins of the field over 7 Mars years. Dune 1 increases in length from 53 m to 93 m. Grid spacing is ~40 m. Also see Animation 1, 3–5.

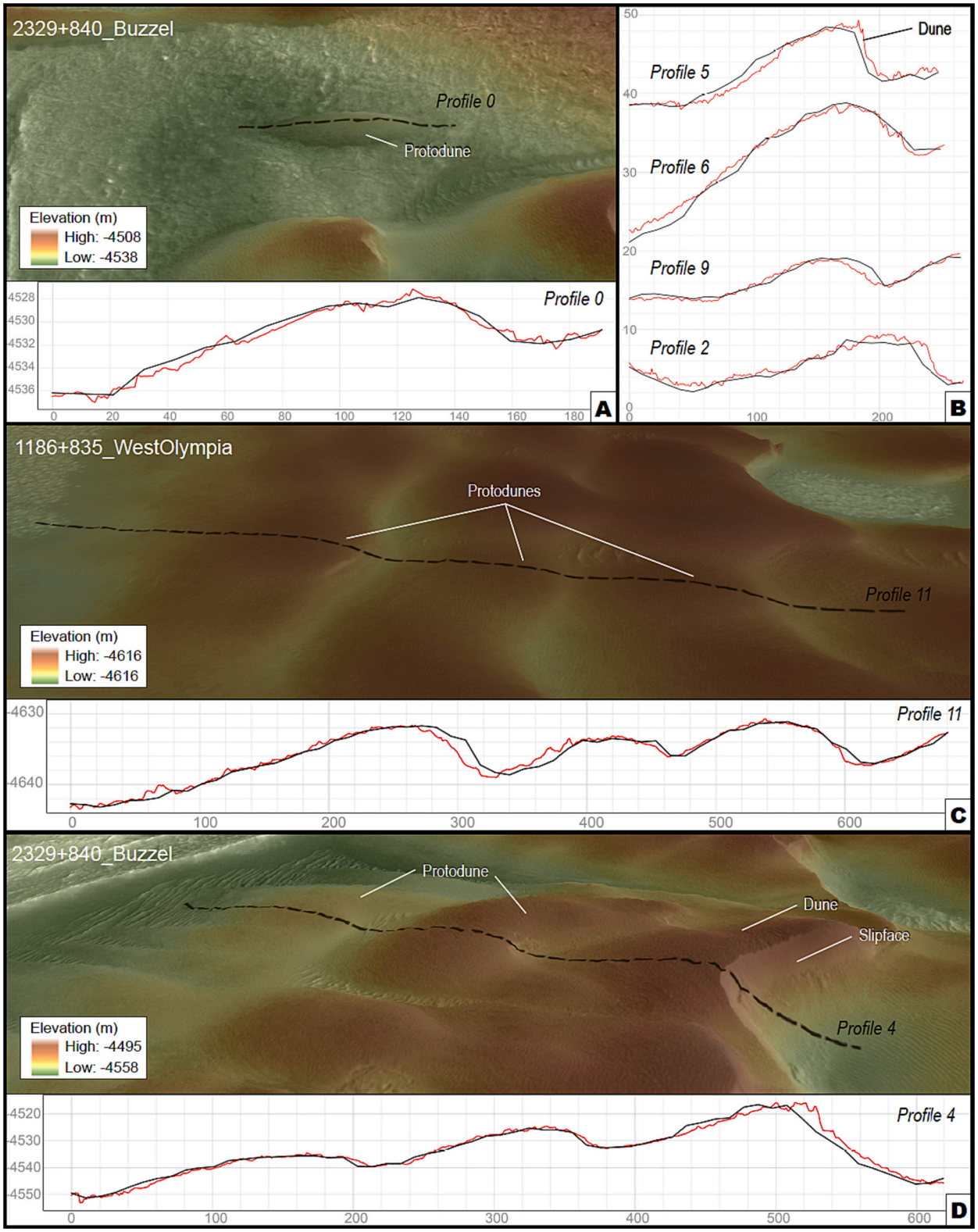

Fig. 7. Topographic elevation profiles and oblique views of sand patches, protodunes, and dunes using HiRISE DTMs - red profiles are using the original 1 m/post elevation data while the smoothed black profiles are downsampled 10 m/post. All profiles are from left to right with downwind to the right, in units of meters. See Supplemental Materials for location information. (A) A sand patch or incipient protodune. (B) Height profiles of three protodunes and one small dune (profile 5) in the study area. (C—D) Profiles of emerging protodunes in the upwind zones of two dune fields. Although some areas are on larger-wavelength ramp topography, which may make defining a base level elevation challenging, protodunes are clearly resolvable at 6 m heights and with 75–200 m wavelengths. (For interpretation of the references to colour in this figure legend, the reader is referred to the web version of this article.)

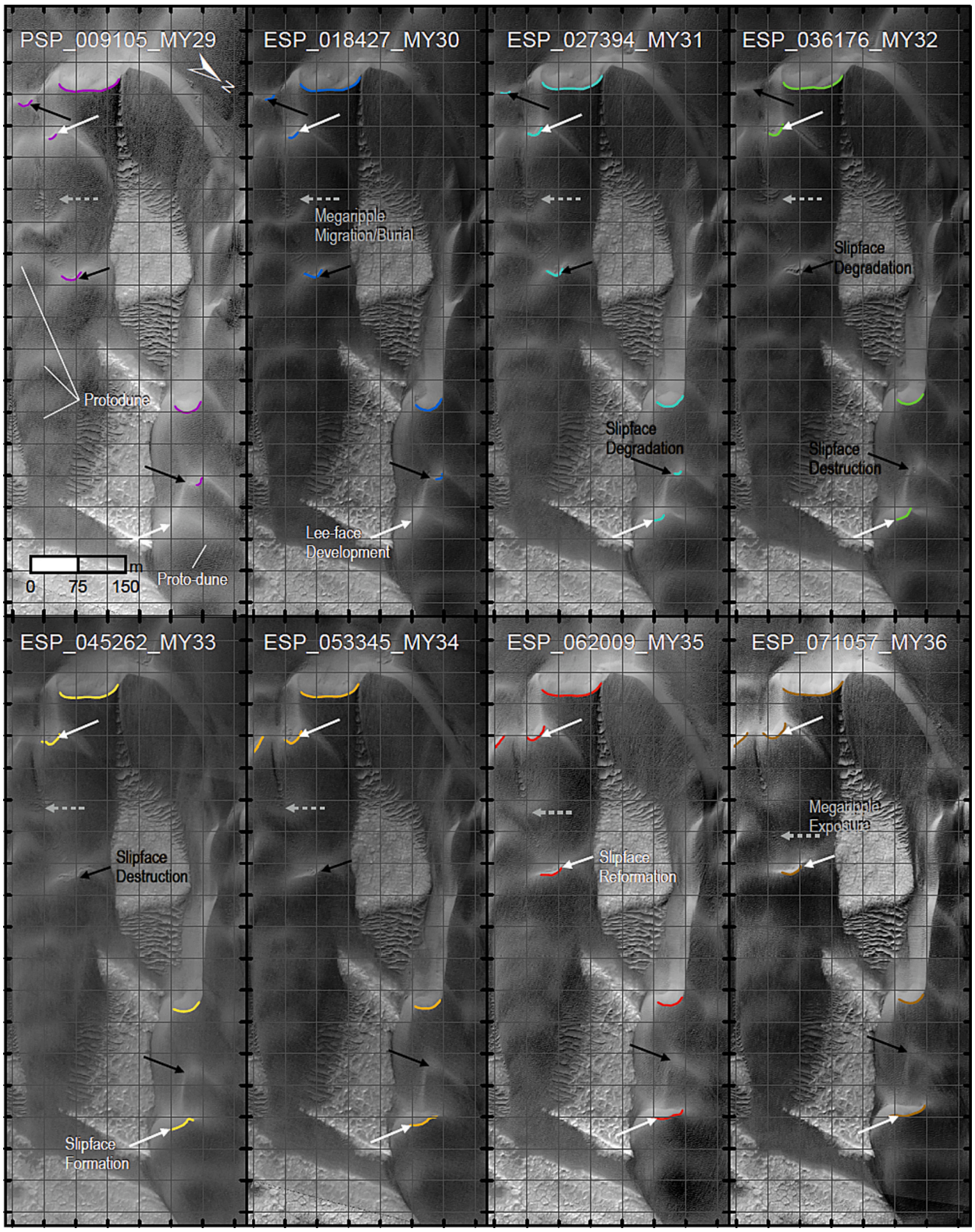

Fig. 8. Sequence of showing protodune to dune formation using 8 HiRISE images over 8 Mars year for one upwind area of the Buzzel dune field. Sequence starts in the top left column (MY29) and proceeds in year to the bottom left (MY36). Colour-coded crest lines were mapped where a resolvable break in the slipface occurred and can be compared from year to year. Slipface formation/expansion (white arrows) and destruction (black arrows), and megaripple burial/migration (gray arrows) are shown. Grid spacing is ~50 m. Also see Animation 4.

repose avalanche slopes where crest brink lines become well defined (Fig. 8, white arrows). Relatively bright south-facing slip faces become large enough to resolve evidence for grainflow (Animation 4–5). This slipface development typically occurs within several dune-wavelengths into the field. Areas with greater sand supply entering a portion of the erg will mature faster and lead to more developed barchan-shaped dunes with stable slipfaces.

The next stage of evolution observed here is the transition from protodune to dune. A protodune is designated for a coherent bedform which has migrated away from its initial nucleation site of deposition and has potential to form a slipface where grain flow or avalanching occurs, at such point it is considered a dune (Kocurek et al., 1992). Protodunes are resolvable in full-resolution HiRISE topography or even downsampled (10 m/post) data showing distinct stoss and lee sides, where crest heights appear to be larger than for many terrestrial protodunes (Fig. 7; See 5.4). As protodunes enter the dune field and obtain greater sand supply they are observed.

This steepening of lee slopes would impact wind flow over the local area with first flow expansion then flow separation (Kocurek et al., 1992). As the incipient dunes enlarge and collect more volume, they protrude into the boundary layer such that they affect downrange sand transport (Jerolmack et al., 2012; Gunn et al., 2020). For example, as the emerging dune slipfaces expand (Fig. 8, white arrows), the adjacent leeward dunes begin to lose their volume and eventually their slipface may collapse (black arrows) - possibly a result of flow separation and declining wind speeds. These smaller dunes which lose their slipfaces are consistent with a minimal size where dune stability can be maintained (Kroy et al., 2002; Pähtz et al., 2013). However, depending on the sediment flux input and where wind flow reattachment occurs a given sand pile may reform its slipface after another few annual cycles. Other protodunes may fail to gain a toehold on becoming a full-fledged dune without sufficient sediment input and wind energy (Animation 4, 5).

Other observations of aeolian evolution include barchan growth and collision. In the case shown in Fig. 6C, the smaller and swifter “Dune 1” is found elongating and increasing in volume as it approaches “Dune 2” (Animation 6). A first order area estimate, as a proxy for volume, showed a rapid increase of 71% over MY29–32 and 69% over MY32–36 for Dune 1. The leeward Dune 2 and 3 areal measurements were all less than ~5% over the same time intervals, although some vertical growth was likely. Meanwhile the 7-m tall Dune 2 rate of migration slows as it impacts and begins to merge with the even slower 20-m tall Dune 3 (Animation 6). Dune 2’s slipface progressively shrinks and degrades between Mars year 29 and 36. Based on transport and lee-face failure rates it is estimated Dune 1 and 2 to be fully absorbed by Dune 3 within a few more annual cycles.

The last stage occurs well into the dune field (~1 km) where increasing larger, crescentic dunes find relative stability in their spacing and height (Fig. 2F, 6A, Animation 8). Dune populations here interact at longer response time scales than the upwind zones and show lesser amounts of incipient slipfaces emerging or collapsing. Evidence for longitudinal sediment transport occurs where barchanoid asymmetry is particularly pronounced to the west (Fig. 8, Animation 1, 4). Increased dune-dune interactions occur downwind that include the lateral linking or merging of crests, and remote transfer of sediment – constructive phenomena which are known in terrestrial dune fields and modeling (Kocurek and Ewing, 2012; Parteli et al., 2014; Ewing et al., 2015). Although the over-steepened lee-faces are reworked by frost-driven alcoves every autumn-winter (Hansen et al., 2011; Diniega et al., 2017), aeolian transport erases most of those changes within a few Mars years. The downwind sections that show slower rates of evolution correspond with the tallest (~60-m-tall) and widest dune (~400-m-wide) topography at the site (Animation 8).

5. Discussion

5.1. Potential factors impacting annual sand transport

Here we discuss the sand flux results in the context to the polar environmental boundary conditions (e.g., topography, seasonal frost, wind speeds). Insight into the question regarding how annual variations in bedform sand fluxes (solid lines) compare with longer term rates (dashed lines) can be viewed in Fig. 9. Some sites show rates with episodic changes, while other appear steady.

5.1.1. Evidence for steady state migration and the role of topography

Two of the sites showed relatively little variability (Fig. 9, cyan and green; sites 1186 + 835 and 2365 + 838) as annual migration and flux rates for these sites tended to stay between ~1–25% of the sites long-baseline measurements, but always within 1 standard deviation (Table 1). The largest year-to-year change in sand flux for these two fields was a decline from ~4.0 m^3m^{-1} yr^{-3} down to 2.5 m^3m^{-1} yr^{-3}. Although West Olympia dunes on average are migrating steadily form year-to-year there is a perceptible increase in fluxes (up to 6×) and change in direction (38°) for the downrange dunes as they narrowly clear the scarp edge, likely due to the funneling of winds (Fig. 2C-2F, S2A). In simpler topographic settings, such as a crater floor where unidirectional winds drive barchan-barchanoid dunes, many studies have documented declining downwind dune fluxes (Bridges et al., 2012; Chojnacki et al., 2017; Runyon et al., 2017; Vaz et al., 2017).

One antecedent similarity for these sites and a possible factor for the relatively low and stable sand fluxes is the geomorphic context. Both West Olympia and Olympia Cavi reentrant sites are similar as they are situated proximal to their sand source and the arcuate topography of the NPLD scarp (Fig. 2C, E, S2A, S2C). In the case of Olympia Cavi, we can test the possible impact of scarp topography on sand fluxes by comparing with the adjacent higher flux site (Fig. 2E). As noted, site 2365+838_OlympiaCavi sits proximal (~800–3000 m) to the head of reentrant Cavi wall, whereas site 2329+840_Buzzel sits ~5 km downwind of its sources scarp with little topography in-between (Fig. 2E-2F, 4B). The Buzzel site had the most sand flux heterogeneity, but also maintained higher annual transport rates than other sites (Fig. 9). When comparing distance to the adjacent upwind scarp (Fig. S4A) there appears to be appreciably lower fluxes for the sites situated near Cavi topography relative to Buzzel. Scarp height, which varied between ~400–700 m, did not appear to impact transport as directly (Fig. S4B). Given the two sites proximity (Fig. 2F, S2B), this vast difference in rates suggests an important role of Cavi scarp topography in diverting or amplifying winds (4B, S4A). However, detailed mesoscale atmospheric simulations, computational fluid dynamic models, and a greater number of study sites would truly be needed to better constrain the influence of topography.

5.1.2. Period of spring defrosting and sediment availability

Defrosting of the north polar erg have been estimated through a variety of approaches and data sets (Hansen et al., 2013; Portyankina et al., 2013; Pommerol et al., 2013; Putzig et al., 2014; Calvin et al., 2015; Diniega et al., 2017; Acharya et al., 2023). While MARCI estimates from daily monitoring allow the most robust method to track the retreat of the massive NPSC and are clearly informative for assessing the rapid brightening of a dune field over the late spring, there are some caveats to this approach. The collection area for brightness values shown on Fig. 5 was a compromise, such that study dunes (Fig. 2C, E, G, S2) were captured, but also a sufficient amount of MARCI pixels were averaged. In certain cases, some non-dune terrain was captured, but even in high sand supply inter-erg areas defrosting sequences are dynamic where many factors (e.g., frost thickness, dune morphology/orientation, wind, etc.; see section 5.2) lead to spatial variations on the order of meters. Rather than a single L_s date for entire dune field, HiRISE temporal analysis show H_2O and CO_2 frost sublimation occurs gradually over the

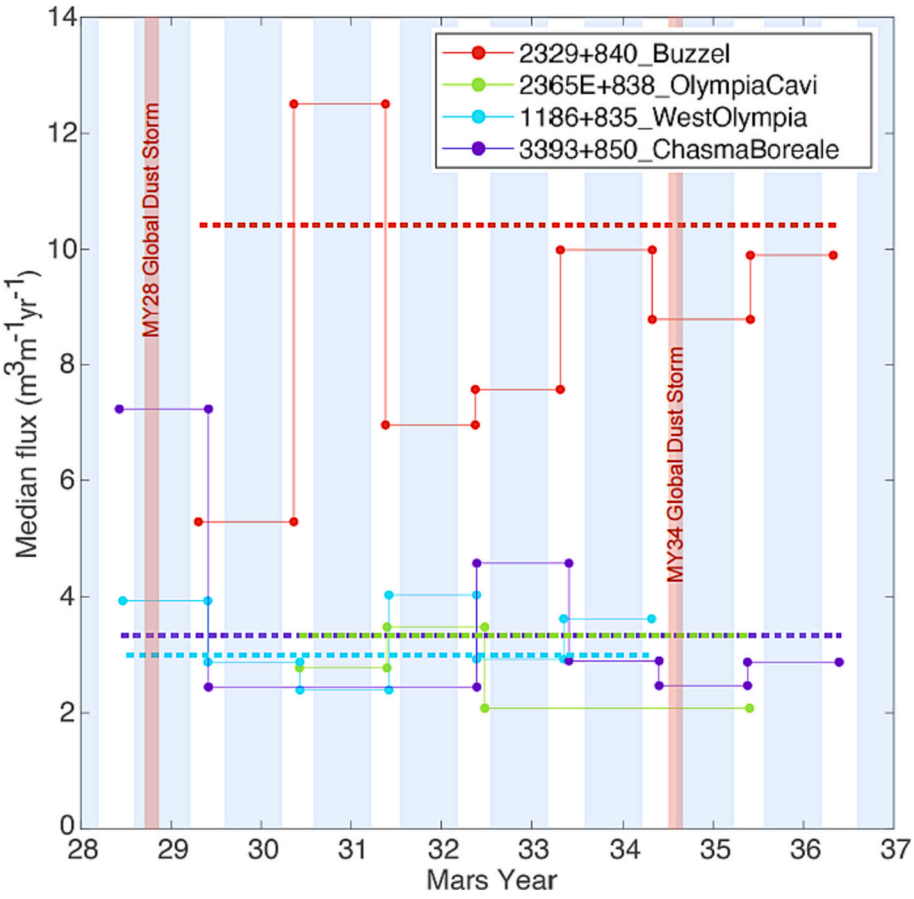

Fig. 9. Cumulative plot of annual sand flux metrics for the 4 study sites where circles correspond with measurements. Median sand fluxes plotted vs. time (Mars year (MY) 28–36) are shown with solid lines. Dashed lines show the long baseline averages. Approximate periods of autumn/winter/spring ice (blue) or global dust events (red) are overlaid. Compare with Fig. 3A-3D and Table 1. (For interpretation of the references to colour in this figure legend, the reader is referred to the web version of this article.)

mid-spring then rapidly when approaching the summer solstice (Hansen et al., 2013; Portyankina et al., 2013; Diniega et al., 2017). The estimated crocus "defrost" dates in Table 2 are therefore more representative of when all frost has been sublimated. Thus, it is important to view these MARCI results in the context of higher resolution, but lower frequency, HiRISE and CTX data.

We hypothesize that sediment availability and the timing of the spring dune field defrost is a critical factor controlling aeolian transport observed in annual image pairs. Sediment availability pertains to whether sand is accessible for aeolian entrainment, which is distinct from sediment supply that is a metric of sand mass and how it changes (Kocurek and Lancaster, 1999). Terrestrial sand availability may be limited due to flooding or vegetation, whereas persistent winter ice may restrict Martian dune sediment and inhibit aeolian transport. The timing of defrosting is critical as late spring (L_s ~ 65°-75°, depending on location; Fig. S4) is when peak annual winds descend the cap in mesoscale simulations, as they are driven by the seasonal CO_2 cap recession (Smith and Spiga, 2018). As wind speeds drop by a factor of two over mid and late summer, the spring prior to the second image in our orthoimage pairs is expected to be where sand transport is the greatest.

At the Buzzel site (Fig. 9, red; 2329+840), sand fluxes from MY29-MY30 are the lowest, while those from MY30-MY31 were far greater than other locations or time periods. All monitoring images here were acquired in the first half of the northern summer (Table 1; L_s 94°-128°), where bedforms have fully defrosted and have been potentially mobile since late spring (L_s ~70°-80°), but sublimation rates will depend on factors including winter-time seasonal frost coverage (Hansen et al., 2013; Portyankina et al., 2013; Acharya et al., 2023). The estimated defrost dates for MY30 and MY31 were not appreciably different based on change of MARCI brightness (Fig. 5, Table 2). However, a late spring defrosting sequence at Buzzel was found to occur in MY30 (compared with MY29 and MY31), based on CO_2 and H_2O frost detections using seasonal HiRISE/CRISM reflectivity measurements (Portyankina et al., 2013). The high levels of MY29 winter CO_2 snowfall, measured by MRO Mars Climate Sounder (Alsaeed et al., 2022), would explain the greater levels of MY30 springtime ice. Anomalously high atmospheric water vapor column abundance was measured in MY30 as compared with other recorded years (MY28-MY33)(Khayat et al., 2019) - this would be consistent with the sublimation of excess water ice during summer solstice. Collectively, we suggest this more extensive ice cover in MY30 would restrict transport during peak wind season for slope winds (Fig. S5) and account for the depressed sand fluxes that year (Fig. 9).

An early spring defrost at Buzzel may help explain the high annual rates over MY30-MY31. Seasonal HiRISE images show dunes are covered in ~90% frost at L_s 65° in MY31 (ESP_025851_2640) and fully defrosted at L_s 81° (ESP_026339_2640) (Diniega et al., 2017), where the latter is similar to the MARCI crocus date of L_s 79.3°, but unfortunately no intermediate images were acquired. However, CTX observation G20_026075_2638 shows the dunes we measured were frost-free at least by L_s 72° in MY31. For context, that would be an earlier spring sequence than other years (certainly compared with MY30) (Hansen et al., 2013; Portyankina et al., 2013), allowing for greater late spring and earlier summer dune advancement to have occurred that year.

The Chasma Boreale site also showed high and variable sand fluxes, providing evidence for years of episodic migration (Fig. 9, purple; 3393+850). Chasma Boreale dunes had the highest fluxes over the Mars

year 28–29 time-step. The most notable event during this period was the MY28 global dust storm, which occurred near the onset of north polar winter (L_s ~260°-310°) when the erg was mantled in ice. In response, it was found that the MY29 north polar seasonal cap was significantly smaller (Fig. 10A) than other years investigated (MY30–35) (Calvin et al., 2015; Acharya et al., 2023). These smaller amounts of estimated ice and earlier defrost dates extended north to three reentrant sites including Chasma Boreale (Fig. 5D, Table 2). The primary cause impacting cap thickness and MY29 springtime sublimation rates has been attributed to the late timing of the MY28 global dust storm that displaced the polar vortex and caused transient warmer polar temperatures (Fig. 10A)(Piqueux et al., 2015b; Guzewich et al., 2016; Acharya et al., 2023). Regardless of the reasons for the smaller MY29 cap, the reduced amount of seasonal ice would result in less frost to sublimate and influenced the erg's sediment state (Fig. 10A). For Chasma Boreale dunes (Fig. 5D, Table 2), this would have resulted in a longer frost-free spring for sand transport between images (MY28 L_s 134°– MY29 L_s 130) and would allow sand to be mobile under peak katabatic flow during late spring (Fig. S4B; L_s ~75°) (Smith and Spiga, 2018). Hence, the MY29 season may not have been windier in Chasma Boreale, but rather the sand was exposed to the atmosphere over a longer period, one that included the faster winds, allowing greater transport to have occurred that year.

Finally, Acharya et al. (2023) found the MY35 north polar seasonal cap was the largest over all the years investigated (MY29-MY35) and was attributed to the lower surface temperatures (Kass et al., 2020) during and after the 2018 MY34 global dust event (Fig. 10B). This larger cap would be consistent with the increased CO_2 snowfall observed over the MY34 winter (Alsaeed et al., 2022). Mars year 35 defrost dates from MARCI were particularly late for Chasma Boreale dunes (Fig. 5, Table 2), which can be confirmed with frost mantling in HiRISE at L_s 85° (Fig. 10B). Although the decrease in fluxes were not as drastic as the increased rates following the MY28 storm were, all three sites that had measurements in MY35 showed coherent declining transport rates compared with adjacent years (Fig. 9). We attribute this to the late defrosting after the maximum wind speeds had occurred.

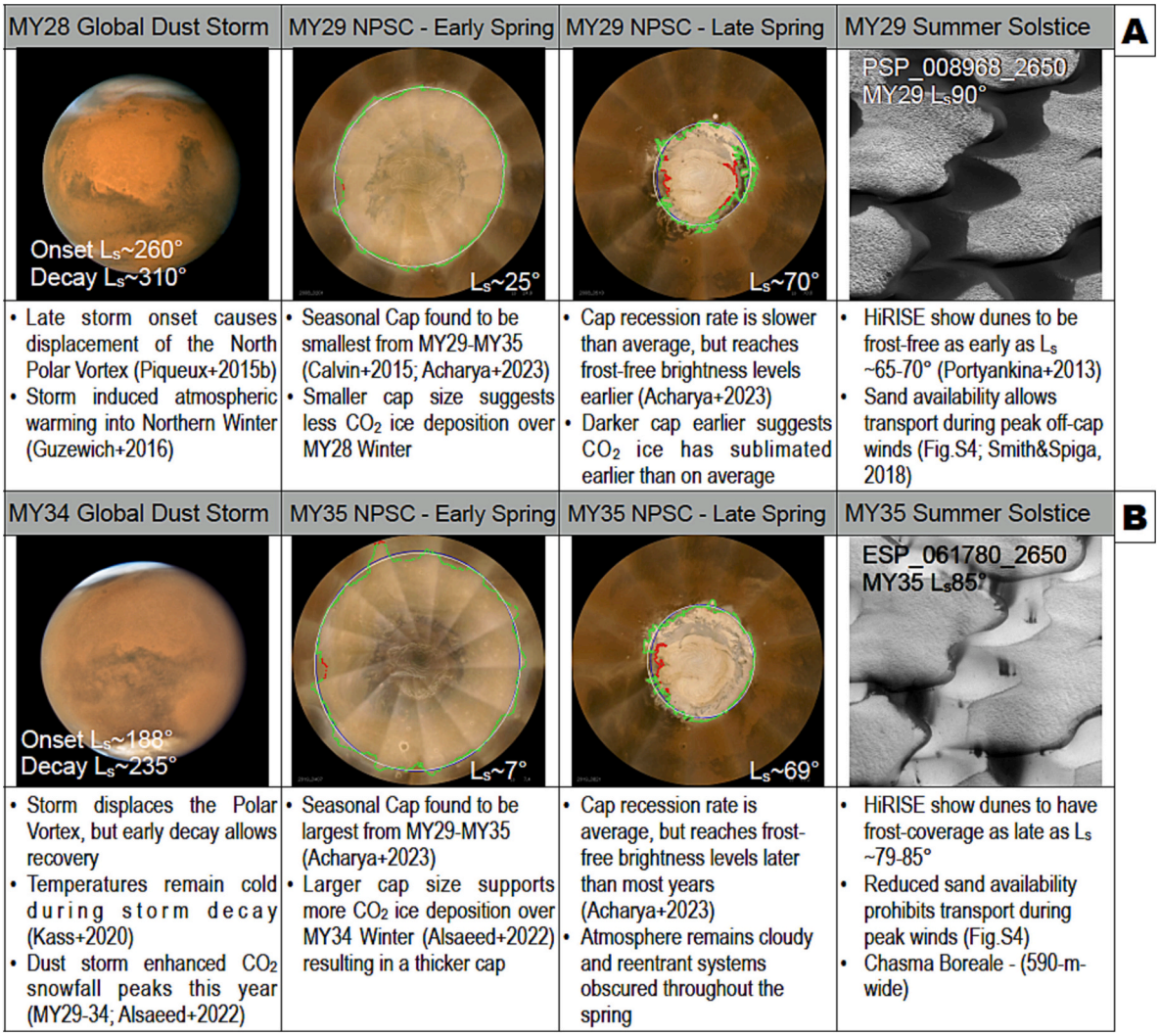

Fig. 10. Proposed scenarios explaining anomalous years of sand fluxes following global dust events for (A) MY28–29 and (B) MY34–35 with descriptions of major observations where time increases from left to right. (Left columns) Global images of Mars during dust storms. Credits: NASA/JPL-Caltech/Hubble Space Telescope. (Center columns) Results of Northern Polar Seasonal Cap (NPSC) mapping from Acharya et al. (2023), where MARCI mosaics show (green) NPSC boundaries and (blue and white) fitted ellipses at the early and late spring (L_s 70°). (Right columns) HiRISE observations of Chasma Boreale dune frost coverage near the Summer Solstice, showing greater coverage in MY35. (For interpretation of the references to colour in this figure legend, the reader is referred to the web version of this article.)

5.2. Contributing factors to the high rates observed at Olympia Cavi "Buzzel" site

Here, we consider potential influencing factors for what maybe the swiftest dunes on Mars (i.e., Buzzel; Fig. 2E, 3B, 9), regardless of the year or image pair (Chojnacki et al., 2019, 2021). This is a worthwhile exercise as sand transport rates are high enough where we can observe dune events (e.g., protodunes, calving, collisions) that have yet to be reported for other dune fields on Mars. For example, the reconstitution timescale (or turnover time), which is the period a bedform takes to migrate its own stoss-to-lee length, is remarkably short at Buzzel - for dune 1 in Fig. 6C that time is 9.8 years, while dune 4 time is 32 years. Often these values are measure or estimated to be an order of magnitude larger (10^2–10^4 Earth-years) at sites in Meridiani Planum, Nili Patera, and other areas (Bridges et al., 2012; Chojnacki et al., 2017; Rubanenko et al., 2022).

The first factor may relate to the dunes' slope and aspect. For example, Buzzel dunes are oriented to the south-southwest allowing near maximum insulation of slipfaces and steep, left (east) flank dune slopes (Fig. 6A). As demonstrated by Hansen et al. (2013), south-facing angle of repose slopes may defrost as early as L_s 45° compared with shallower (10°) slopes at L_s 75°. This orientation allows slipface avalanching to occur in mid-spring, even when stoss-side slopes were frosted (Diniega et al., 2017). It can also be found that the upwind zone (northeast) of the dune field (Fig. 6A) typically defrosts earlier than larger dunes to the south. This earlier spring defrosting of this zone would allow a longer total wind season for the rapid protodune evolution to occur (Fig. 8, Animations 1 vs. 8). More generally, it is noted the Cavi scarp-geometry that is parallel to the dune field front and lacks prominent topography (Fig. 2F) allow spring-summer off-cap katabatic sublimation winds to maximize their impact on the landscape.

Finally, a distinct longitudinal asymmetry was found in the derived wintertime CO_2 ice cloud column densities, where the north polar minima (longitudes 180°-300°) includes the Buzzel site (233°) and most of Olympia Undae (Alsaeed et al., 2022). This polar vortex pattern was stable across MY29-MY35 of MRO Mars Climate Sounder data (N. Alsaeed, personal communication 2023), which would suggest reduced mid-altitude (10–60 km) CO_2 snowfall in Olympia Undae and less springtime ice to sublimate relative to other longitudes (Fig. 2B). This lower density of CO_2 snowfall clouds is a manifestation of the greater elevation of Olympia Undae that propagates into the atmosphere as a stationary wave (Alsaeed et al., 2022).

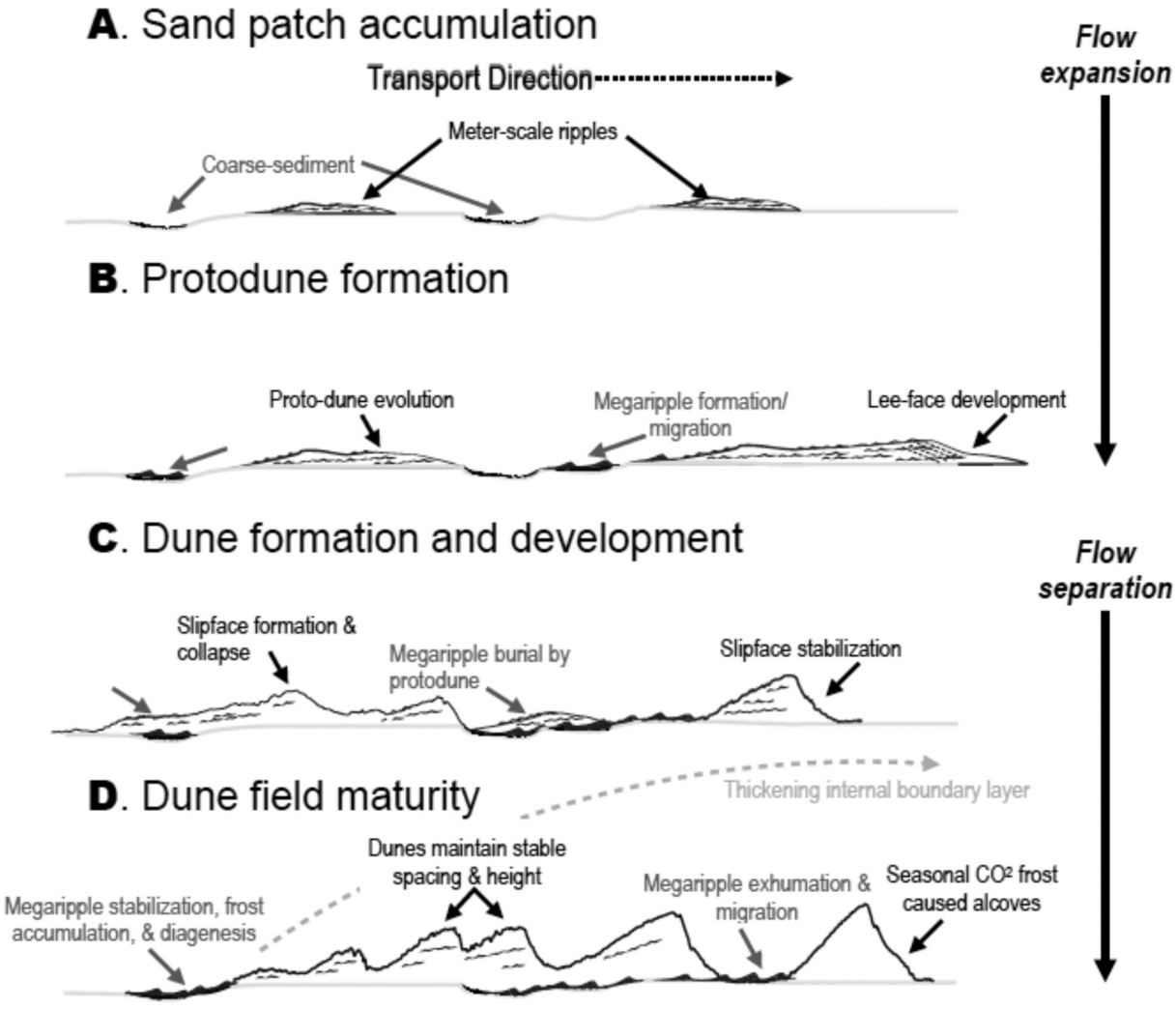

Fig. 11. Stages of aeolian system evolution in the north polar reentrant systems. (A) Fine sand accumulates into patches, which quickly develop meter-scale ripples. Coarse sediment accumulates in depressions or patch margins. (B) Protodunes rapidly migrate and develop angle of repose lee-side slopes where sand supply is sufficient. Megaripples collect and migrate. (C) Slipfaces form, collapse, and reform as adjacent dunes compete for sand supply. Larger, downwind dunes expand and maintain slipfaces with increased grainflow. Megaripples migrate along dune margins or become buried. (D) Mature dunes stabilize their spacing and height. Seasonal alcoves form in autumn/winter but are erased by aeolian deposition/erosion of the lee-face. Megaripples may remobilize following exhumation, whereas others become stabilized and rendered immobile. Also see Fig. 7, 8 & Animation 4. Compare with Kocurek et al. (1992) for terrestrial dunes evolution.

5.3. Stages of aeolian system evolution in the Martian polar reentrants

Here we discuss the envisioned phases of aeolian bedform initiation and development in the north polar erg. Although it stems from specific examples at the Buzzel site, all elements are applicable to other reentrant systems. In the observations, we can recognize most of the stages of terrestrial dune development initially outlined by Kocurek et al. (1992) (sand patches, wind-ripple protodunes and dunes) for coastal settings and expanded upon by Phillips et al. (2019) and Gadal et al. (2020) at White Sands Dune Field, New Mexico (USA), but with some important modifications. Based on the geomorphic, stratigraphic, and temporal observations we suggest the following sequence of events to explain how local aeolian systems evolve (Fig. 11):

A. Sand that is sourced from Cavi units is delivered to lower scarps via mass wasting and aeolian transport (Fig. S3). Irregular rippled sand patches form in spring and summer on the plains below scarps, which begin to migrate downwind (Fig. 11A, 6A, S3B). Particle size partitioning may occur with the accumulation of coarser particles in depressions or patch margins.
B. As sediment supply increases, protodunes 1–6 m tall collect and seasonally migrate (Fig. 7, 8). Protodunes develop lee-side slopes with grain flow as their topography induces secondary flow expansion. Calving events may occur as sand piles migrate across rugged topography causing sand escape in the form of (unresolved) decimeter-wavelength impact and larger meter-scale ripples that reform into new sand patches, protodunes, and eventually dunes (Fig. 6A, B, Animation 1). Coarser sediment forms asymmetrical megaripples in the pathways of greater sediment transport.
C. With increased sand supply over multiple Mars years, protodunes evolve into dunes with slipface formation (Fig. 8, 11C). The incipient dunes, now ~10 m tall, induce lee-side secondary flow separation, which reduces transport for downwind bedforms. Based on terrestrial examples the leeside scouring of downrange bedforms, brought on by turbulence, may enhance slipface formation and size (Phillips et al., 2019). This decreased sediment influx and wind energy, along with erosion by winter-time ice, may cause some small dunes to sustain slipface collapse (Animation 2, 4). Adjacent dunes and protodunes compete for sand supply, where collisions, absorptions, and lateral linking of dunes may occur (Fig. 6C). Downwind dunes with greater volume (typically >10-m tall) expand and maintain slipfaces with increased grainflow (Animations 5). Megaripples migrate along dune margins, become buried, and either become remobilized or stabilized over winter (Fig. 4, 5).
D. Over decadal time scales increasingly large and stable barchanoid dunes maintain their spacing and height (Fig. 2F, 11D). This morphologic stability comes at the cost of slower migration rates and less dramatic annual change, as compared with the smaller, swifter upwind bedforms (Animations 1 vs. 8). These decaying sand flux profiles are related to the thickening internal boundary layer, caused by rough topography the dunes present to atmospheric flow (Gunn et al., 2020). Alcoves and avalanches form on steep slipfaces in autumn/winter by CO_2 slabs but are largely erased following one or more migration seasons (Diniega et al., 2017). Megaripples may remobilize following exhumation, whereas others become fully stabilized, rendered immobile, and eventual lithified into the polar record (Chojnacki et al., 2021). Likewise, dune foresets may be slowly deposited and cemented along the erg base which finally get exposed as cross-bedding (Ewing et al., 2010).

All these stages are in the context of drastic polar seasonal conditions, where all bedform surfaces are blanketed by autumn/winter CO_2/H_2O ice, sublimation of springtime frost, and subject to wind season throughout frost-free periods over late spring and summer. During mid and late summer, wind speeds drop by a factor of two or more, reducing the shear stress near active dunes and slowing migration (Fig. S4) (Smith and Spiga, 2018). In locations of low aeolian activity, bedforms that are static over long periods of times may become significantly impacted by cryospheric processes. For example, ground ice may penetrate into erg surfaces several 10's of centimeters over winter, which can manifest in the partial burial of ripples and megaripples by ice leading to the stabilization by ice-cemented sand just below the surface (Putzig et al., 2014; Chojnacki et al., 2021). Other polar bedforms may show evidence for cross-stratified ice or degraded morphologies (weathered, cracked, rounded or "boxy" crests) indicative of prolonged modification (Brothers and Kocurek, 2018; Chojnacki et al., 2021). More ancient examples include cross-bedded strata and bounding surfaces found along Cavi scarps that are interpreted as various components of an ancient aeolian sand sea (Brothers et al., 2018; Nerozzi and Holt, 2019).

However, these high latitude paleobedform occurrences are distinct from the quickly evolving aeolian systems at the head of the polar reentrants (Fig. 2, 11). While we have documented bedform formation (dune and meter scale ripples) over 3–5 Mars years (Fig. 5, 6) these examples are not likely representative for many or most locations on Mars. For example, a global survey of dune activity estimated sand fluxes for north polar sites to be 50% greater than the average for Mars (Chojnacki et al., 2019) with non-polar dune migration rates often 3–15 times lower (Bridges et al., 2012; Silvestro et al., 2013; Vaz et al., 2017). Thus, the aeolian system evolution in Olympia Undae and Chasma Boreale over 8 Mars years provides some insight into how slower dune fields evolve over much greater timescales.

5.4. Martian vs. terrestrial protodune development and dimensions

Terrestrial studies of protodune dynamics have evolved from serendipitous field observations to annual LiDAR measurements to landscape-scale experiments (Bagnold, 1941; Kocurek et al., 1992; Nield et al., 2011; Ping et al., 2014; Baddock et al., 2018; Phillips et al., 2019; Gadal et al., 2020). These studies have collectively provided insight into the spatial and temporal transition of flat sand patches to slipface-bearing dunes. An understanding of the mechanisms that forms these nascent bedforms on extraterrestrial planetary surfaces is in a preliminary stage with a few studies noting their existence (Bourke, 2010; Ewing et al., 2015; Li et al., 2018; Chojnacki et al., 2019).

Although an immersive analysis of Martian protodune formation is outside the scope of this paper we can point to a few revelations found herein. It's been documented that terrestrial protodunes and their precursor sand patches emerge at 5 cm to ~1 m heights, can gain amplitude in the matter of hours, and show consistent dynamics with linear stability theory (Baddock et al., 2018; Phillips et al., 2019; Gadal et al., 2020; Delorme et al., 2023). In contrast, Martian protodunes displayed in Fig. 7 are 1–2 orders of magnitude taller than examples on Earth, although their topographic profiles and shapes are relatively similar. Smaller protodunes were not evident in the study area although they may be transient. Superposed meter scale ripples contribute to some of their greater relief, which are always resolvable on the sandy bedforms we surveyed (Fig. 6-8). These "large ripples" are typically 10–40 cm in height (Bridges et al., 2013; Lapotre et al., 2018), which alone would be larger than some terrestrial protodunes. Although it's difficult to assess hourly growth rates, early summer observations at Buzzel (MY35, L_s 95°–105 (Chojnacki et al., 2021)) demonstrate distinct protodune translation and shape changes over the matter of a few weeks. Improved quantification of protodune sand fluxes and propagation velocity may be possible for Mars, which could be compared with protodunes at White Sands (Phillips et al., 2019; Gadal et al., 2020). Acquiring height variation measurements, to constrain growth rate, is more challenging but possible, as it will require repeated well-controlled HiRISE DTMs (Sutton et al., 2022).

6. Conclusions

We conducted an intensive campaign to document and characterize bedform evolution of several dune fields in the north polar erg. These annual and seasonal observations cover most of the MRO mission to date and include data returned from Mars year 28–36 (2006–2022). This research and revelations it produced could not have been completed without the continual and regular monitoring by the MRO HiRISE team and support staff (Landis et al., 2023).

Sand fluxes at certain reentrant sites showed extreme heterogeneity with years of maximum aeolian transport occurring after the series minima. The years of highest flux measurements were attributed to the early spring defrosting of dunes (Mars years 29 & 31), which allowed sand to be mobile for longer durations including periods of peak winds near the end of spring. Chasma Boreale dunes experienced the greatest sand transport in MY29 following the smallest seasonal cap observed by MRO (MY29-MY35). The smaller cap size and lesser amounts of MY29 polar ice, which we propose limits sand availability and fluxes, has been linked to the late onset of the Mars year 28 global dust storm that caused transient vortex warming over northern winter. In contrast, late spring defrosting in MY30 was found to have had a role in restricting sand transport at the Buzzel site, causing its lowest annual fluxes. All sites showed similar minima or low annual flux in MY35 following the larger seasonal cap size, greater CO_2 snowfall, and lower surface temperatures related to the Mars year 34 global dust storm and its early timing. Climate factors such as global dust storms that may impact seasonal polar ice appear to have a crucial role in sand availability and transport for polar dunes; these factors demonstrate the complex interplay of boundary conditions on Mars.

In contrast to sites with transport heterogeneity, two sites that are situated more proximal to Cavi scarp slopes were observed with stable and moderate year-to-year sand fluxes. We also observed cases where Cavi topography directed or influenced sediment transport azimuth and magnitude. These examples of steady-state migration are despite annual changes in seasonal ice, winter-time CO_2 snowfall, and periods of polar storms.

The high flux aeolian systems at the Olympia Cavi reentrant site Buzzel evolved with dunes, ripples, and megaripples rapidly migrating in annual time steps. Protodunes gain sand volume, develop slipfaces, and transition into fully formed barchans several meters tall within 3–5 annual cycles. Other occurrences of slipface collapse, dune collision, dune calving, and ripple formation were also observed and to our knowledge are novel to planetary science.

Dune migration rates here were up to 15 times faster that of dunes located at lower latitudes. This is despite the limited transport over northern winter and spring, where sand is mantled in frost and ice. The contributing boundary conditions to the Buzzel site having the swiftest bedforms yet detected on Mars (Fig. 2; Chojnacki et al., 2019, 2021) include: the sand dunes line-source geometry, strong scarp winds, and lower winter accumulation of CO_2 snowpack (less spring-time frost to sublimate) across much of higher elevation Olympia Undae.

Other factors such as the frequency of polar storms, variations in global temperatures, or rates of sediment supply input from Cavi units are all additional considerations for annual change of sand fluxes. These results provide insight into the extreme conditions at the north polar region and how aeolian and cryospheric processes can conspire to drive rapid landscape evolution on Mars.

Supplementary data to this article can be found online at https://doi.org/10.1016/j.icarus.2023.115863.

Declaration of Competing Interest

The authors declare that they have no known competing financial interests or personal relationships that could have appeared to influence the work reported in this paper.

Data availability

All data used for this investigation can be found at the HiRISE Planetary Data System (PDS) website (https://hirise.lpl.arizona.edu/PDS/). More specifically, McEwen (2006) for Reduced Data Records and McEwen (2009) for Digital Terrain Models. Additional data available via the Planetary Data System Imaging and Geosciences nodes (https://pds-imaging.jpl.nasa.gov/volumes/mro.html) and the Geosciences node (https://pds-geosciences.wustl.edu/missions/mep/index.htm). All map-projected HiRISE images in figures are courtesy NASA/JPL/University of Arizona, and map-projected CTX images (Malin, 2007) are courtesy NASA/JPL/MSSS/University of Arizona.

Acknowledgments

For M.C., S.S., and I.S. this research was supported in part by NASA Mars Data Analysis Program Grant 80NSSC21K1096 and the HiRISE/MRO mission. D.A.V. acknowledge CITEUC's support (UID/Multi/00611/2021&POCI-01-0145-FEDER-006922), FCT (Grant CEECIND/02981/2017), and the Laboratory for Advanced Computing at University of Coimbra for providing computing resources. We would like to thank HiRISE operations staff with assistance in targeting and Kris Akers for DTM production. Thanks to N. Alsaeed for her feedback on CO_2 snowfall in the region. M.C. performed his work on this manuscript in Lakewood Colorado, which is located on the traditional territory of the Cherokee, Ute, Sioux, and other Native Americans. We honor the past, present, and future generations of these tribes on their land. Supporting information is available in the online version of the paper, including supplemental Animations 1-8, Figs. S1-S5, and Table S1 including HiRISE images and DTMs with hyperlinks.

References

Acharya, P.J., Smith, I.B., Calvin, W.M., 2023. Tracking the northern seasonal cap retreat of Mars using computer vision. Icarus 390, 115295. https://doi.org/10.1016/j.icarus.2022.115295.

Alsaeed, N.R., Hayne, P.O., Concepcion, V., 2022. Dust-Driven polar vortex dynamics and snowfall from Mars climate sounder observations. In: Presented at the 53rd Lunar and Planetary Science Conference. Lunar and Planetary Institute, Houston p. Abstract #1792.

Ayoub, F., Avouac, J.-P., Newman, C.E., Richardson, M.I., Lucas, A., Leprince, S., Bridges, N.T., 2014. Threshold for sand mobility on Mars calibrated from seasonal variations of sand flux. Nat. Commun. 5.

Baddock, M.C., Nield, J.M., Wiggs, G.F.S., 2018. Early-stage aeolian protodunes: Bedform development and sand transport dynamics: early-stage aeolian protodunes. Earth Surf. Process. Landf. 43, 339–346. https://doi.org/10.1002/esp.4242.

Bagnold, R.A., 1941. The Physics of Blown Sand and Desert Dunes. Methuen, London.

Baker, M.M., Lapotre, M.G.A., Minitti, M.E., Newman, C.E., Sullivan, R., Weitz, C.M., Rubin, D.M., Vasavada, A.R., Bridges, N.T., Lewis, K.W., 2018. The Bagnold dunes in southern summer: active sediment transport on Mars observed by the curiosity rover. Geophys. Res. Lett. 45, 8853–8863. https://doi.org/10.1029/2018GL079040.

Baker, M.M., Newman, C.E., Sullivan, R., Minitti, M.E., Edgett, K.S., Fey, D., Ellison, D., Lewis, K.W., 2022. Diurnal variability in Aeolian sediment transport at Gale crater. JGR Planets 127. https://doi.org/10.1029/2020JE006734.

Balme, M., Berman, D.C., Bourke, M.C., Zimbelman, J.R., 2008. Transverse Aeolian ridges (TARs) on Mars. Geomorphology 101, 703–720. https://doi.org/10.1016/j.geomorph.2008.03.011.

Banks, M.E., Fenton, L.K., Bridges, N.T., Geissler, P.E., Chojnacki, M., Runyon, K.D., Silvestro, S., Zimbelman, J.R., 2018. Patterns in mobility and modification of middle- and high-latitude southern hemisphere dunes on Mars. J. Geophys. Res.: Planets. https://doi.org/10.1029/2018JE005747.

Becerra, P., Smith, I.B., Hibbard, S., Andres, C., Bapst, J., Bramson, A.M., Buhler, P.B., Coronato, A., Diniega, S., Emmett, J., Grau Galofre, A., Herny, C., Kahre, M., Paul Knightly, J., Nerozzi, S., Pascuzzo, A., Portyankina, G., Rabassa, J., Tamppari, L.K., Titus, T.N., Whitten, J., Yoldi, Z., 2021. Past, present, and future of Mars polar science: outcomes and outlook from the 7th international conference on Mars polar science and exploration. Planet. Sci. J. 2, 209. https://doi.org/10.3847/PSJ/ac19a5.

Bell, J.F., Wolff, M.J., Malin, M.C., Calvin, W.M., Cantor, B.A., Caplinger, M.A., Clancy, R.T., Edgett, K.S., Edwards, L.J., Fahle, J., Ghaemi, F., Haberle, R.M., Hale, A., James, P.B., Lee, S.W., McConnochie, T., Noe Dobrea, E., Ravine, M.A., Schaeffer, D., Supulver, K.D., Thomas, P.C., 2009. Mars reconnaissance orbiter Mars color imager (MARCI): instrument description, calibration, and performance. J. Geophys. Res. 114 https://doi.org/10.1029/2008JE003315.

Bourke, M., Edgett, K., Cantor, B., 2008. Recent aeolian dune change on Mars. Geomorphology 94, 247–255. https://doi.org/10.1016/j.geomorph.2007.05.012.

Bourke, M.C., 2010. Barchan dune asymmetry: Observations from Mars and earth. Icarus 205, 183–197. https://doi.org/10.1016/j.icarus.2009.08.023.
Bridges, N.T., Geissler, P.E., McEwen, A.S., Thomson, B.J., Chuang, F.C., Herkenhoff, K. E., Keszthelyi, L.P., Martínez-Alonso, S., 2007. Windy Mars: a dynamic planet as seen by the HiRISE camera. Geophys. Res. Lett. 34 https://doi.org/10.1029/2007GL031445.
Bridges, N.T., Bourke, M.C., Geissler, P.E., Banks, M.E., Colon, C., Diniega, S., Golombek, M.P., Hansen, C.J., Mattson, S., McEwen, A.S., Mellon, M.T., Stantzos, N., Thomson, B.J., 2011. Planet-wide sand motion on Mars. Geology 40, 31–34. https://doi.org/10.1130/G32373.1.
Bridges, N.T., Ayoub, F., Avouac, J.-P., Leprince, S., Lucas, A., Mattson, S., 2012. Earth-like sand fluxes on Mars. Nature 485, 339–342. https://doi.org/10.1038/nature11022.
Bridges, N.T., Geissler, P., Silvestro, S., Banks, M., 2013. Bedform migration on Mars: current results and future plans. Aeolian Res. 9, 133–151. https://doi.org/10.1016/j.aeolia.2013.02.004.
Brothers, S.C., Kocurek, G., 2018. The transitional depositional environment and sequence stratigraphy of Chasma Boreale. Icarus 308, 27–41. https://doi.org/10.1016/j.icarus.2017.08.038.
Brothers, S.C., Kocurek, G., Holt, J.W., 2018. Sequence architecture of the cavi unit, Chasma Boreale, Mars. Icarus 308, 42–60. https://doi.org/10.1016/j.icarus.2017.06.024.
Byrne, S., Murray, B.C., 2002. North polar stratigraphy and the paleo-erg of Mars. J. Geophys. Res.: Planets 107, 11. https://doi.org/10.1029/2001JE001615.
Calvin, W.M., James, P.B., Cantor, B.A., Dixon, E.M., 2015. Interannual and seasonal changes in the north polar ice deposits of Mars: observations from MY 29–31 using MARCI. Icarus 251, 181–190. https://doi.org/10.1016/j.icarus.2014.08.026.
Cantor, B.A., Pickett, N.B., Malin, M.C., Lee, S.W., Wolff, M.J., Caplinger, M.A., 2019. Martian dust storm activity near the Mars 2020 candidate landing sites: MRO-MARCI observations from Mars years 28–34. Icarus 321, 161–170. https://doi.org/10.1016/j.icarus.2018.10.005.
Chojnacki, M., Johnson, J.R., Moersch, J.E., Fenton, L.K., Michaels, T.I., Bell III, J.F., 2015. Persistent aeolian activity at Endeavour crater, Meridiani Planum, Mars; new observations from orbit and the surface. Icarus 251, 275–290. https://doi.org/10.1016/j.icarus.2014.04.044.
Chojnacki, M., Urso, A.C., Fenton, L.K., Michaels, T.I., 2017. Aeolian dune sediment flux heterogeneity in Meridiani Planum, Mars. Aeolian Res. 26, 73–88. https://doi.org/10.1016/j.aeolia.2016.07.004.
Chojnacki, M., Banks, M., Urso, A., 2018. Wind-driven erosion and exposure potential at Mars 2020 rover candidate-landing sites. J. Geophys. Res. Planets 123, 468–488. https://doi.org/10.1002/2017JE005460.
Chojnacki, M., Banks, M.E., Fenton, L.K., Urso, A.C., 2019. Boundary condition controls on the high-sand-flux regions of Mars. Geology. https://doi.org/10.1130/G45793.1.
Chojnacki, M., Vaz, D.A., Silvestro, S., Silva, D.C.A., 2021. Widespread Megaripple activity across the north polar ergs of Mars. J. Geophys. Res. Planets 126. https://doi.org/10.1029/2021JE006970.
Chojnacki, M., Vaz, D.A., Silvestro, S., Silva, D.C.A., 2022. Annual Variability of Dune Field Fluxes on Mars. In: 53rd Lunar and Planetary Science Conference. Lunar and Planetary Institute, Houston p. Abstract #2064.
Delorme, P., Nield, J.M., Wiggs, G.F.S., Baddock, M.C., Bristow, N.R., Best, J.L., Christensen, K.T., Claudin, P., 2023. Field evidence for the initiation of isolated Aeolian sand patches. Geophys. Res. Lett. 50 https://doi.org/10.1029/2022GL101553 e2022GL101553.
Diniega, S., Hansen, C.J., Allen, A., Grigsby, N., Li, Z., Perez, T., Chojnacki, M., 2017. Dune-slope activity due to frost and wind throughout the north polar erg. Mars. Geol. Soc. Lond. 467, 95–114. https://doi.org/10.1144/SP467.6.
Diniega, S., Bramson, A.M., Buratti, B., Buhler, P., Burr, D.M., Chojnacki, M., Conway, S. J., Dundas, C.M., Hansen, C.J., McEwen, A.S., Lapôtre, M.G.A., Levy, J., Mc Keown, L., Piqueux, S., Portyankina, G., Swann, C., Titus, T.N., Widmer, J.M., 2021. Modern Mars' geomorphological activity, driven by wind, frost, and gravity. Geomorphology 380, 107627. https://doi.org/10.1016/j.geomorph.2021.107627.
Diniega, S., Burr, D.M., Chojnacki, M., Lapôtre, M.G.A., Swann, C., 2022. Martian Dunes: A crucial record of present and past Mars surface environment and aeolian processes, in: Treatise on Geomorphology. Elsevier, pp. 617–636. doi:https://doi.org/10.1016/B978-0-12-818234-5.00177-2.
Eastwood, E.N., Kocurek, G., Mohrig, D., Swanson, T., 2012. Methodology for reconstructing wind direction, wind speed and duration of wind events from aeolian cross-strata: methodology for wind reconstruction. J. Geophys. Res. 117, n/a-n/a. https://doi.org/10.1029/2012JF002368.
Ewing, R.C., Kocurek, G., 2010. Aeolian dune-field pattern boundary conditions. Geomorphology 114, 175–187. https://doi.org/10.1016/j.geomorph.2009.06.015.
Ewing, R.C., Peyret, A.-P.B., Kocurek, G.A., Bourke, M., 2010. Dune field pattern formation and recent transporting winds in the Olympia Undae dune field, north polar region of Mars. J. Geophys. Res. 115, E08005. https://doi.org/10.1029/2009JE003526.
Ewing, R.C., McDonald, G.D., Hayes, A.G., 2015. Multi-spatial analysis of aeolian dune-field patterns. Geomorphology 240, 44–53. https://doi.org/10.1016/j.geomorph.2014.11.023.
Fanara, L., Gwinner, K., Hauber, E., Oberst, J., 2019. Present-day erosion rate of north polar scarps on Mars due to active mass wasting. Icarus 113434. https://doi.org/10.1016/j.icarus.2019.113434.
Fenton, L.K., 2020. Updating the global inventory of dune fields on Mars and identification of many small dune fields. Icarus 352, 114018. https://doi.org/10.1016/j.icarus.2020.114018.
Fishbaugh, K.E., Head, J.W., 2005. Origin and characteristics of the Mars north polar basal unit and implications for polar geologic history. Icarus 174, 444–474. https://doi.org/10.1016/j.icarus.2004.06.021.
Gadal, C., Narteau, C., Ewing, R.C., Gunn, A., Jerolmack, D., Andreotti, B., Claudin, P., 2020. Spatial and temporal development of incipient dunes. Geophys. Res. Lett. 47 https://doi.org/10.1029/2020GL088919.
Geissler, P.E., Wilgus, J.T., 2017. The morphology of transverse aeolian ridges on Mars. Aeolian Res. 26, 63–71. https://doi.org/10.1016/j.aeolia.2016.08.008.
Geissler, P.E., Johnson, J.R., Sullivan, R., Herkenhoff, K., Mittlefehldt, D., Fergason, R., Ming, D., Morris, R., Squyres, S., Soderblom, L., Golombek, M., 2008. First in situ investigation of a dark wind streak on Mars. J. Geophys. Res. 113 https://doi.org/10.1029/2008JE003102.
Greeley, R., Iversen, J.D., 1985. Wind as a Geological Process on Earth, Mars, Venus and Titan. Cambridge Univ. Press, New York.
Greeley, R., Lancaster, N., Lee, S.W., Thomas, P.C., 1992. Martian Aeolian processes, sediments and features. In: Kieffer, H.H., Jakosky, B.M., Snyder, C.W., Matthews, M. S. (Eds.), Mars, Space Science Series. University of Arizona Press, Tucson, pp. 730–766.
Gunn, A., Schmutz, P., Wanker, M., Edmonds, D.A., Ewing, R.C., Jerolmack, D.J., 2020. Macroscopic flow disequilibrium over Aeolian dune fields. Geophys. Res. Lett. 47 https://doi.org/10.1029/2020GL088773.
Guzewich, S.D., Toigo, A.D., Waugh, D.W., 2016. The effect of dust on the martian polar vortices. Icarus 278, 100–118. https://doi.org/10.1016/j.icarus.2016.06.009.
Hansen, C.J., Bourke, M., Bridges, N.T., Byrne, S., Colon, C., Diniega, S., Dundas, C., Herkenhoff, K., McEwen, A., Mellon, M., Portyankina, G., Thomas, N., 2011. Seasonal Erosion and restoration of Mars' northern polar dunes. Science 331, 575–578. https://doi.org/10.1126/science.1197636.
Hansen, C.J., Byrne, S., Portyankina, G., Bourke, M., Dundas, C., McEwen, A., Mellon, M., Pommerol, A., Thomas, N., 2013. Observations of the northern seasonal polar cap on Mars: I. Spring sublimation activity and processes. Icarus 225, 881–897. https://doi.org/10.1016/j.icarus.2012.09.024.
Hansen, C.J., Diniega, S., Bridges, N., Byrne, S., Dundas, C., McEwen, A., Portyankina, G., 2015. Agents of change on Mars' northern dunes: CO2 ice and wind. Icarus 251, 264–274. https://doi.org/10.1016/j.icarus.2014.11.015.
Hayward, R.K., 2011. Mars global digital dune database (MGD3): north polar region (MC-1) distribution, applications, and volume estimates. Earth Surf. Process. Landf. 36, 1967–1972. https://doi.org/10.1002/esp.2219.
Herkenhoff, K.E., Byrne, S., Russell, P.S., Fishbaugh, K.E., McEwen, A.S., 2007. Meter-scale morphology of the north polar region of Mars. Science 317, 1711–1715.
Horgan, B., Bell, J.F., 2012. Widespread weathered glass on the surface of Mars. Geology. https://doi.org/10.1130/G32755.1.
Howard, A., 2000. The role of Eolian processes in forming surface features of the Martian polar layered deposits. Icarus 144, 267–288. https://doi.org/10.1006/icar.1999.6305.
Jerolmack, D.J., Ewing, R.C., Falcini, F., Masteller, C., Phillips, C., Reitz, M.D., Buynevich, I., 2012. Internal boundary layer model for the evolution of desert dune fields. Nat. Geosci. 5, 206–209. https://doi.org/10.1038/ngeo1381.
Kass, D.M., Schofield, J.T., Kleinböhl, A., McCleese, D.J., Heavens, N.G., Shirley, J.H., Steele, L.J., 2020. Mars climate sounder observation of Mars' 2018 global dust storm. Geophys. Res. Lett. 47 https://doi.org/10.1029/2019GL083931.
Khayat, A.S.J., Smith, M.D., Guzewich, S.D., 2019. Understanding the water cycle above the north polar cap on Mars using MRO CRISM retrievals of water vapor. Icarus 321, 722–735. https://doi.org/10.1016/j.icarus.2018.12.024.
Kirk, R.L., Howington-Kraus, E., Rosiek, M.R., Anderson, J.A., Archinal, B.A., Becker, K. J., Cook, D.A., Galuszka, D.M., Geissler, P.E., Hare, T.M., Holmberg, I.M., Keszthelyi, L.P., Redding, B.L., Delamere, W.A., Gallagher, D., Chapel, J.D., Eliason, E.M., King, R., McEwen, A.S., 2008. Ultrahigh resolution topographic mapping of Mars with MRO HiRISE stereo images: meter-scale slopes of candidate Phoenix landing sites. J. Geophys. Res. 113 https://doi.org/10.1029/2007JE003000.
Kocurek, G., Lancaster, N., 1999. Aeolian system sediment state: theory and Mojave Desert Kelso dune field example. Sedimentology 46, 505–515. https://doi.org/10.1046/j.1365-3091.1999.00227.x.
Kocurek, G., Townsley, M., Havholm, K., Sweet, 1992. Dune and dune-field development on Padre Island, Texas, with implications for Interdune deposition and water-table-controlled accumulation. SEPM JSR 62. https://doi.org/10.1306/D4267974-2B26-11D7-8648000102C1865D.
Kocurek, G.A., Ewing, R.C., 2012. Source-to-sink: An earth/Mars comparison of boundary conditions for Aeolian dune systems. In: Grotzinger, J.P., Grotzinger, J.P., Milliken, R.E. (Eds.), Sedimentary Geology of Mars. SEPM Special Publication. SEPM (Society for Sedimentary Geology), Tulsa, Okla, p. 18.
Kocurek, G.A., Ewing, R.C., Mohrig, D., 2010. How do bedform patterns arise? New views on the role of bedform interactions within a set of boundary conditions. Earth Surf. Process. Landf. 35, 51–63. https://doi.org/10.1002/esp.1913.
Kroy, K., Sauermann, G., Herrmann, H.J., 2002. Minimal model for sand dunes. Phys. Rev. Lett. 88, 054301 https://doi.org/10.1103/PhysRevLett.88.054301.
Lancaster, N., 2009. Dune morphology and dynamics. In: Parsons, AnthonyJ, Abrahams, AtholD (Eds.), Geomorphology of Desert Environments, vol. Chapter 18. Springer, Netherlands, pp. 557–595.
Landis, M.E., Acharya, P.J., Alsaeed, N.R., Andres, C., Becerra, P., Calvin, W.M., et al., 2023. Polar science results from Mars Reconnaissance Orbiter: Multiwavelength, multiyear insights. Icarus 115794. https://doi.org/10.1016/j.icarus.2023.115794.
Langevin, Y., 2005. Summer evolution of the north polar cap of Mars as observed by OMEGA/Mars express. Science 307, 1581–1584. https://doi.org/10.1126/science.1109438.

Lapotre, M.G.A., Ewing, R.C., Lamb, M.P., Fischer, W.W., Grotzinger, J.P., Rubin, D.M., Lewis, K.W., Ballard, M.J., Day, M., Gupta, S., Banham, S.G., Bridges, N.T., Des Marais, D.J., Fraeman, A.A., Grant, J.A., Herkenhoff, K.E., Ming, D.W., Mischna, M. A., Rice, M.S., Sumner, D.A., Vasavada, A.R., Yingst, R.A., 2016. Large wind ripples on Mars: a record of atmospheric evolution. Science 353, 55–58. https://doi.org/10.1126/science.aaf3206.

Lapotre, M.G.A., Ewing, R.C., Weitz, C.M., Lewis, K.W., Lamb, M.P., Ehlmann, B.L., Rubin, D.M., 2018. Morphologic diversity of Martian ripples: implications for large-ripple formation. Geophys. Res. Lett. https://doi.org/10.1029/2018GL079029.

Li, C., Dong, Z., Chen, G., Yang, J., Cui, X., Li, J., 2018. Qaidam Basin as an analog for linear dune formation in Chasma Boreale, Mars: a comparative analysis. Geomorphology 322, 29–40. https://doi.org/10.1016/j.geomorph.2018.08.033.

Malin, M.C., 2007. MRO Context Camera Experiment Data Record Level 0 V1.0. https://doi.org/10.17189/1520266.

McEwen, A.S., 2006. MRO Mars High Resolution Image Science Experiment RDR V1.0. https://doi.org/10.17189/1520303.

McEwen, A.S., 2009. MRO Mars High Resolution Imaging Science Experiment DTM V1.0. https://doi.org/10.17189/1520227.

McEwen, A.S., Eliason, E.M., Bergstrom, J.W., Bridges, N.T., Hansen, C.J., Delamere, W. A., Grant, J.A., Gulick, V.C., Herkenhoff, K.E., Keszthelyi, L., Kirk, R.L., Mellon, M.T., Squyres, S.W., Thomas, N., Weitz, C.M., 2007. Mars reconnaissance Orbiter's high resolution imaging science experiment (HiRISE). J. Geophys. Res. 112 https://doi.org/10.1029/2005JE002605.

Nerozzi, S., Holt, J.W., 2019. Buried ice and sand caps at the north pole of Mars: revealing a record of climate change in the Cavi unit with SHARAD. Geophys. Res. Lett. https://doi.org/10.1029/2019GL082114, 2019GL082114.

Nield, J.M., Wiggs, G.F.S., Squirrell, R.S., 2011. Aeolian sand strip mobility and protodune development on a drying beach: examining surface moisture and surface roughness patterns measured by terrestrial laser scanning. Earth Surf. Process. Landf. 36, 513–522. https://doi.org/10.1002/esp.2071.

Pähtz, T., Kok, J.F., Parteli, E.J.R., Herrmann, H.J., 2013. Flux saturation length of sediment transport. Phys. Rev. Lett. 111, 218002 https://doi.org/10.1103/PhysRevLett.111.218002.

Parteli, E.J.R., Durán, O., Bourke, M.C., Tsoar, H., Pöschel, T., Herrmann, H., 2014. Origins of barchan dune asymmetry: insights from numerical simulations. Aeolian Res. 12, 121–133. https://doi.org/10.1016/j.aeolia.2013.12.002.

Phillips, J.D., Ewing, R.C., Bowling, R., Weymer, B.A., Barrineau, P., Nittrouer, J.A., Everett, M.E., 2019. Low-angle eolian deposits formed by protodune migration, and insights into slipface development at White Sands dune field, New Mexico. Aeolian Res. 36, 9–26. https://doi.org/10.1016/j.aeolia.2018.10.004.

Ping, L., Narteau, C., Dong, Z., Zhang, Z., Courrech du Pont, S., 2014. Emergence of oblique dunes in a landscape-scale experiment. Nat. Geosci. 7, 99–103. https://doi.org/10.1038/ngeo2047.

Piqueux, S., Byrne, S., Kieffer, H.H., Titus, T.N., Hansen, C.J., 2015a. Enumeration of Mars years and seasons since the beginning of telescopic exploration. Icarus 251, 332–338. https://doi.org/10.1016/j.icarus.2014.12.014.

Piqueux, S., Kleinböhl, A., Hayne, P.O., Kass, D.M., Schofield, J.T., McCleese, D.J., 2015b. Variability of the martian seasonal CO2 cap extent over eight Mars years. Icarus 251, 164–180. https://doi.org/10.1016/j.icarus.2014.10.045.

Pommerol, A., Appéré, T., Portyankina, G., Aye, K.-M., Thomas, N., Hansen, C.J., 2013. Observations of the northern seasonal polar cap on Mars III: CRISM/HiRISE observations of spring sublimation. Icarus 225, 911–922. https://doi.org/10.1016/j.icarus.2012.08.039.

Portyankina, G., Pommerol, A., Aye, K.-M., Hansen, C.J., Thomas, N., 2013. Observations of the northern seasonal polar cap on Mars II: HiRISE photometric analysis of evolution of northern polar dunes in spring. Icarus 225, 898–910. https://doi.org/10.1016/j.icarus.2012.10.017.

Putzig, N.E., Mellon, M.T., Herkenhoff, K.E., Phillips, R.J., Davis, B.J., Ewer, K.J., Bowers, L.M., 2014. Thermal behavior and ice-table depth within the north polar erg of Mars. Icarus 230, 64–76. https://doi.org/10.1016/j.icarus.2013.07.010.

Roback, K.P., Runyon, K., Newman, C., Avouac, J.-P., 2022. Multi-year measurements of ripple and dune migration on Mars: implications for the wind regime and sand transport. Icarus 380, 114966. https://doi.org/10.1016/j.icarus.2022.114966.

Rubanenko, L., Gunn, A., Pérez-López, S., Fenton, L.K., Ewing, R.C., Soto, A., Lapôtre, M. G.A., 2022. Global Surface Winds and Aeolian Sediment Pathways on Mars from the Morphology of Barchan Dunes (preprint). Preprints. https://doi.org/10.22541/essoar.167169649.93488411/v1.

Runyon, K.D., Bridges, N.T., Ayoub, F., Newman, C.E., Quade, J.J., 2017. An integrated model for dune morphology and sand fluxes on Mars. Earth Planet. Sci. Lett. 457, 204–212. https://doi.org/10.1016/j.epsl.2016.09.054.

Russell, P., Thomas, N., Byrne, S., Herkenhoff, K., Fishbaugh, K., Bridges, N., Okubo, C., Milazzo, M., Daubar, I., Hansen, C., McEwen, A., 2008. Seasonally active frost-dust avalanches on a north polar scarp of Mars captured by HiRISE. Geophys. Res. Lett. 35, L23204. https://doi.org/10.1029/2008GL035790.

Silvestro, S., Fenton, L.K., Vaz, D.A., Bridges, N.T., Ori, G.G., 2010. Ripple migration and dune activity on Mars: evidence for dynamic wind processes. Geophys. Res. Lett. 37, L20203.

Silvestro, S., Vaz, D.A., Ewing, R.C., Rossi, A.P., Fenton, L.K., Michaels, T.I., Flahaut, J., Geissler, P.E., 2013. Pervasive aeolian activity along rover Curiosity's traverse in Gale crater, Mars. Geology 41, 483–486. https://doi.org/10.1130/G34162.1.

Silvestro, S., Vaz, D.A., Yizhaq, H., Esposito, F., 2016. Dune-like dynamic of Martian Aeolian large ripples: longitudinal large ripples on Mars. Geophys. Res. Lett. 43, 8384–8389. https://doi.org/10.1002/2016GL070014.

Silvestro, S., Chojnacki, M., Vaz, D.A., Cardinale, M., Yizhaq, H., Esposito, F., 2020. Megaripple migration on Mars. J. Geophys. Res. Planets. https://doi.org/10.1029/2020JE006446.

Smith, I.B., Holt, J.W., 2010. Onset and migration of spiral troughs on Mars revealed by orbital radar. Nature 465, 450–453. https://doi.org/10.1038/nature09049.

Smith, I.B., Spiga, A., 2018. Seasonal variability in winds in the north polar region of Mars. Icarus 308, 188–196. https://doi.org/10.1016/j.icarus.2017.10.005.

Smith, I.B., Holt, J.W., Spiga, A., Howard, A.D., Parker, G., 2013. The spiral troughs of Mars as cyclic steps: the spiral troughs of Mars. J. Geophys. Res. Planets 118, 1835–1857. https://doi.org/10.1002/jgre.20142.

Smith, I.B., Diniega, S., Beaty, D.W., Thorsteinsson, T., Becerra, P., Bramson, A.M., Clifford, S.M., Hvidberg, C.S., Portyankina, G., Piqueux, S., Spiga, A., Titus, T.N., 2018. 6th international conference on Mars polar science and exploration: conference summary and five top questions. Icarus 308, 2–14. https://doi.org/10.1016/j.icarus.2017.06.027.

Su, S., Fanara, L., Zhang, X., Hauber, E., Gwinner, K., Oberst, J., 2023. Searching for the sources of ice block falls at the martian north polar scarps. Icarus 390, 115321. https://doi.org/10.1016/j.icarus.2022.115321.

Sullivan, R., Kok, J.F., 2017. Aeolian saltation on Mars at low wind speeds: low speed Aeolian saltation on Mars. J. Geophys. Res.: Planets. https://doi.org/10.1002/2017JE005275.

Sullivan, R., Banfield, D., Bell, J.F., Calvin, W., Fike, D., Golombek, M., Greeley, R., Grotzinger, J., Herkenhoff, K., Jerolmack, D., Malin, M., Ming, D., Soderblom, L.A., Squyres, S.W., Thompson, S., Watters, W.A., Weitz, C.M., Yen, A., 2005. Aeolian processes at the Mars exploration rover Meridiani Planum landing site. Nature 436, 58–61. https://doi.org/10.1038/nature03641.

Sullivan, R., Arvidson, R., Bell, J.F., Gellert, R., Golombek, M., Greeley, R., Herkenhoff, K., Johnson, J., Thompson, S., Whelley, P., Wray, J., 2008. Wind-driven particle mobility on Mars: insights from Mars exploration rover observations at "El Dorado" and surroundings at Gusev crater. J. Geophys. Res. 113 https://doi.org/10.1029/2008JE003101.

Sullivan, R., Baker, M., Newman, C., Turner, M., Schieber, J., Weitz, C., Hallet, B., Ellison, D., Minitti, M., 2022. The Aeolian environment in Glen Torridon, Gale crater, Mars. JGR Planets 127. https://doi.org/10.1029/2021JE007174.

Sutton, S.S., Chojnacki, M., McEwen, A.S., Kirk, R.L., Dundas, C.M., Schaefer, E.I., Conway, S.J., Diniega, S., Portyankina, G., Landis, M.E., Baugh, N.F., Heyd, R., Byrne, S., Tornabene, L.L., Ojha, L., Hamilton, C.W., 2022. Revealing active Mars with HiRISE digital terrain models. Remote Sens. 14, 2403. https://doi.org/10.3390/rs14102403.

Tanaka, K., Rodriguez, J., Skinnerjr, J., Bourke, M., Fortezzo, C., Herkenhoff, K., Kolb, E., Okubo, C., 2008. North polar region of Mars: advances in stratigraphy, structure, and erosional modification. Icarus 196, 318–358. https://doi.org/10.1016/j.icarus.2008.01.021.

Thomas, P., Weitz, C., 1989. Sand dune materials and polar layered deposits on Mars. Icarus 81, 185–215. https://doi.org/10.1016/0019-1035(89)90133-4.

Urso, A., Chojnacki, M., Vaz, D.A., 2018. Dune-Yardang interactions in Becquerel crater, Mars: dune-Yardang interactions in Becquerel crater, Mars. J. Geophys. Res.: Planets. https://doi.org/10.1002/2017JE005465.

Vaz, D.A., Silvestro, S., Sarmento, P.T.K., Cardinale, M., 2017. Migrating meter-scale bedforms on Martian dark dunes: are terrestrial aeolian ripples good analogues? Aeolian Res. 26, 101–116. https://doi.org/10.1016/j.aeolia.2016.08.003.

Vaz, D.A., Silvestro, S., Chojnacki, M., Silva, D.C.A., 2023. Constraining the mechanisms of aeolian bedform formation on Mars through a global morphometric survey. Earth Planet. Sci. Lett. 614, 118196 https://doi.org/10.1016/j.epsl.2023.118196.

Wang, H., Fisher, J.A., 2009. North polar frontal clouds and dust storms on Mars during spring and summer. Icarus 204, 103–113. https://doi.org/10.1016/j.icarus.2009.05.028.

Wilson, I.G., 1973. Ergs. Sediment. Geol. 10, 77–106. https://doi.org/10.1016/0037-0738(73)90001-8.

Zurek, R.W., Smrekar, S.E., 2007. An overview of the Mars reconnaissance orbiter (MRO) science mission. J. Geophys. Res. 112, E05S01. https://doi.org/10.1029/2006JE002701.